

Official Journal of Turkish Society of Magnetic Resonance

CRMRI

Current Research in MRI

Circle of Willis Variations Detected by Time of Flight Magnetic Resonance Imaging Angiography in Eastern Anatolia Region
Fadime Güven, İsmail Malkoç, Ahmet Tuğrul Akkuş

The Diffusion Tensor Imaging Features in the Visual Pathways of Patients with Cavernous Sinus Meningioma Treated by Gamma Knife Radiosurgery
Hafize Otçu Timur, Alpay Alkan, Mustafa Aziz Hatiboğlu, İsmail Yurtsever, Kerime Akdur, Özlem Toluk, Mehmet Hakan Seyithanoğlu

Deep Learning-Based Diagnosis of Chondromalacia Patella from Magnetic Resonance Images
Okan Demirtaş, Sümeyra Kuş, Semih Demirel, Habib Eser Akkaya, Oktay Yıldız, Ömer Kazcı

Effect of Breast Fibroglandular Tissue Density in Tumor Visualization and Characterization on Diffusion MRI
Hatice Ayça Ata Korkmaz, Sibel Kul, İlker Eyüboğlu, Mehmet Şükrü Oğuz, İsmet Miraç Çakır, Süleyman Bekircavuşoğlu

Editor in Chief

Mecit Kantarcı 

Department of Radiology, Erzincan Binali Yıldırım University, Faculty of Medicine; Atatürk University, Faculty of Medicine, Erzincan, Erzurum, Türkiye

Editors

Abdominal Radiology

Aytekin Oto 

The University of Chicago, Department of Radiology, Chief Physician, Head of the Faculty Practice Plan and Dean for Clinical Affairs, Chicago, USA

Murat Danacı 

Department of Radiology, Ondokuz Mayıs University, Faculty of Medicine, Samsun, Türkiye

Breast Radiology

Serap Gültekin 

Department of Radiology, Gazi University, Faculty of Medicine, Ankara, Türkiye

Cardiac Radiology

Memduh Dursun 

Department of Radiology, İstanbul University, İstanbul Faculty of Medicine, İstanbul, Türkiye

Cihan Duran 

Department of Diagnostic and Interventional Imaging, The University of Texas, McGovern Medical School, Texas, USA

Emergency Radiology

Mehmet Ruhi Onur 

Department of Radiology, Hacettepe University Faculty of Medicine Hospital, Ankara, Türkiye

Engineer Group

Esin Öztürk Işık 

Biomedical Engineering, Boğaziçi University, İstanbul, Türkiye

Head & Neck Radiology

Nafi Aygün 

Department of Radiology, Johns Hopkins University School of Medicine, Baltimore, Maryland, USA

Hatice Gül Hatipoğlu 

Department of Radiology, Health Science University, Gulhane Faculty of Medicine, Ankara Bilkent City Hospital, Ankara, Türkiye

Musculoskeletal Radiology

Nil Tokgöz 

Department of Radiology, Gazi University, Faculty of Medicine, Ankara, Türkiye

Neuroradiology Radiology


Alpay Alkan 

Department of Radiology, Bezmialem Vakıf University, Faculty of Medicine, İstanbul, Türkiye

Pediatric Radiology

Korgün Koral 

Department of Radiology, University of Texas Southwestern Medical Center, Dallas, TX, USA

Süreyya Burcu Görkem 

Department of Pediatric Radiology, Adana State Hospital, Adana, Türkiye

Thorax Radiology

Polat Koşucu 

Department of Radiology, Karadeniz Teknik University, Faculty of Medicine, Trabzon, Türkiye

Biostatistical Consultant

Sonay Aydın 

Department of Radiology, Erzincan Binali Yıldırım University, Faculty of Medicine, Erzincan, Türkiye



General Manager
İbrahim KARA

Publications Director
Deniz KAYA

Finance Coordinator
Gözde DOĞAN

Publications Coordinators

Nisanur ATICI
Şeref Mert GÜCÜN
Lütfiye ÇETİN
Batuhan KARA
Tabita TOPARLAK
Şevval AKKAYA

Web Coordinator

Ayça Nur SEZEN

Web Assistant

Ozan ŞAHİN

Contact

Address: Halaskargazi Mah. Halaskar-gazi Cad. No: 38 -66E İç Kapı No: 215
Şişli, İstanbul, Türkiye.
Phone: +90 212 217 17 00
E-mail: info@avespublishing.com

About the Current Research in MRI

Current Research in MRI is a peer reviewed, open access, on-line-only journal published by the Turkish Society of Magnetic Resonance.

Current Research in MRI is a triannual journal that is published in English in April, August, and December.

Indexing

Current Research in MRI is covered in the following indexing database;

- EBSCO
- DOAJ
- China National Knowledge Infrastructure (CNKI)

All content published in the journal is permanently archived in Portico.

Aims, Scope, and Audience

Current Research in MRI aims to publish studies of the highest scientific and clinical value. It also encourages the submission of high-quality research in the field of radiology.

Current Research in MRI covers a wide range of topics related to radiology.

Current Research in MRI publishes original articles, reviews, case reports, and letters to the editor that are prepared in accordance with ethical guidelines.

The target audience of the journal includes healthcare professionals, physicians, and researchers who are interested in or working in the field of radiology.

You can reach the current version of the instructions to authors at <https://curremr.com/EN>

Editor in Chief: Mecit Kantarcı

Address: Department of Radiology, Erzincan Binali Yıldırım University School of Medicine, Erzincan, Türkiye
E-mail: akkanrad@hotmail.com

Publisher: Turkish Society of Magnetic Resonance

Address: Konak Mah. 858. Sok. No: 2 Çakıroğlu İş Hanı Kat: 5
Daire: 55 Konak / İzmir, Türkiye

Publishing Services: AVES

Address: Halaskargazi Mah. Halaskargazi Cad. No: 38 -66E İç Kapı No: 215 Şişli, İstanbul, Türkiye.
Phone: +90 212 217 17 00
E-mail: info@avespublishing.com
Webpage: www.avespublishing.com

CONTENTS

ORIGINAL ARTICLES

- 1 Circle of Willis Variations Detected by Time of Flight Magnetic Resonance Imaging Angiography in Eastern Anatolia Region
Fadime Güven, İsmail Malkoç, Ahmet Tuğrul Akkuş
- 7 The Diffusion Tensor Imaging Features in the Visual Pathways of Patients with Cavernous Sinus Meningioma Treated by Gamma Knife Radiosurgery
Hafize Otçu Temur, Alpay Alkan, Mustafa Aziz Hatiboğlu, İsmail Yurtsever, Kerime Akdur, Özlem Toluk, Mehmet Hakan Seyithanoğlu
- 12 Deep Learning-Based Diagnosis of Chondromalacia Patella from Magnetic Resonance Images
Okan Demirtaş, Sümeyra Kuş, Semih Demirel, Habib Eser Akkaya, Oktay Yıldız, Ömer Kazcı
- 22 Effect of Breast Fibroglandular Tissue Density in Tumor Visualization and Characterization on Diffusion MRI
Hatice Ayça Ata Korkmaz, Sibel Kul, İlker Eyüboğlu, Mehmet Şükrü Oğuz, İsmet Miraç Çakır, Süleyman Bekirçavuşoğlu

Circle of Willis Variations Detected by Time of Flight Magnetic Resonance Imaging Angiography in Eastern Anatolia Region

Fadime Güven¹ , İsmail Malkoç² , Ahmet Tuğrul Akkuş³ 

¹Department of Radiology, Atatürk University Faculty of Medicine, Erzurum, Türkiye

²Department of Anatomy, Düzce University Faculty of Medicine, Erzurum, Türkiye

³Department of Radiology, Erzurum City Hospital, Erzurum, Türkiye

Cite this article as: Güven F, Malkoç İ, Akkuş AT. Circle of Willis variations detected by TOF magnetic resonance imaging angiography in the Eastern Anatolia region. *Current Research in MRI*, 2025;4(1):1-6.

Corresponding author: Ahmet Tuğrul, e-mail: akkustugrul@gmail.com

Received: April 22, 2025 **Revision Requested:** May 13, 2025 **Last Revision Received:** May 21, 2025 **Accepted:** June 04, 2025 **Publication Date:** August 22, 2025

DOI: 10.5152/CurrResMRI.2025.25120



Content of this journal is licensed under a Creative Commons Attribution-NonCommercial 4.0 International License.

Abstract

Objective: The purpose of the study was to determine variations in the circle of Willis in the Eastern Anatolia Region with TOF magnetic resonance imaging angiography.

Methods: Two hundred fifty cases between the ages of 18 and 50, who applied to the department for cranial magnetic resonance angiography (MRA) examination and had no specific symptoms, were included in the study. Study data were obtained with 1.5 T and 3T MR (Magnetom Skyra; Siemens Healthcare, Erlangen, Germany) devices.

Results: Typical polygonal structure was seen in 80 cases (32%) and arteria communicans anterior (AComA) aplasia was seen in 4 cases (1.62%). The incidence of right and left anterior cerebral artery (ACA) A1 aplasia and hypoplasia were 11 (4.4%), 5 (2%), 14 (5.5%), and 6 (2.4%), respectively. ACA trifurcation was detected in 19 (7.6%), azygos ACA in 2 (0.8%), and bi-hemispheric ACA in 4 (1.6%). Right and left arteria communicans posterior (AComP) aplasia and hypoplasia were detected in 42 (16.8%), 32 (12.8%), 25 (10%), and 26 (10.4%), respectively. Right arteria cerebri posterior (ACP) fetal configuration was determined in 26 (10.4%), left in 15 (6%), and bilateral in 16 (6.4%). Basilar artery fenestration and persistent trigeminal artery were detected in 3 cases (1.2%). Right and left vertebral artery hypoplasia was determined in 20 (8%) and 14 (5.6%) cases, respectively.

Conclusion: The anatomical determination of the normal structure and variations of the Willis polygon with TOF MRA, which is a non-invasive imaging method that does not require radiation exposure and contrast material, revealed that the typical polygonal structure where all the arteries are located was detected at a rate of 32%. The most frequently detected variations were aplasia/hypoplasia, and they were seen most frequently in AComP (between 10% and 16.8%). The most frequently detected variation in anterior circulation was ACA trifurcation (7.6%), and it was similar to the literature.

Keywords: Anatomic variation, circle of Willis, magnetic resonance angiography, magnetic resonance imaging

INTRODUCTION

The circle of Willis is a ring of vessels that form a connection between anterior and posterior circulation. Both internal carotid arteries (ICAs) give off an ophthalmic artery and form anterior cerebral artery (ACA) and middle cerebral artery (MCA). The anterior communicating artery (ACom) connects bilateral ACAs. The posterior communicating artery (PCom) connects the MCA with the posterior cerebral arteries (PCAs). The basilar artery (BA) divides into 2 to form PCAs.¹

The circle of Willis is the basic structure that ensures constant and regular blood flow to the brain in order to protect it from ischemia. The studies of the British anatomist Sir Thomas Willis in the 17th century forms the basis of the anatomical knowledge one has about the brain and vascular anatomy today.² Today, the studies of Yaşargil and Rhoton form the basis of the vascular anatomy of the modern central nervous system.^{3,4} Although there are detailed studies of each artery forming the circle in the literature, studies that include the whole circle are relatively few. In addition, while there are few studies on the circle of Willis in the adult population in the Turkish society in the literature, no such study has been found for the Eastern Anatolia region.

Collateral circulation in circle of Willis is important in maintaining adequate cerebral blood flow in case of obstructive arterial diseases. There are 2 types of collateral vessels: extracranial and intracranial collateral vessels. Intracranial collateral vessels are formed by primary collaterals which connect the arterial segments of the circle of Willis and secondary collaterals such as leptomeningeal vessels that form after an insult when primary collaterals are not sufficient.

There are studies reporting higher frequency of incomplete circle of Willis in migraine patients in particular in migraine patients with aura.⁵ Thus variations in the posterior circulation are found to be a contributing factor to stroke in migraine patients.⁶

The purpose of the study is to determine incidence of anatomical variants in Eastern Anatolia Region and compare it to the literature.

MATERIAL AND METHODS

Patient Group

The single-institution, prospective study was approved by the institutional ethics committee of Atatürk University (Ethics Committee number: B.30.2.ATA.0.01.00/277, date: May 30, 2019). Written informed consent forms were signed by all study participants.

In this study, it is aimed to prospectively investigate the presence and localization of circle of Willis variations in TOF magnetic resonance angiography (MRA) images obtained for various indications between 2019 and 2020. Two hundred fifty cases were included between the ages of 18 and 50 without specific symptoms in the study. Exclusion criteria as follows: patients with brain surgery or aneurysmal coil embolization, patients younger than 18, and images without adequate quality to assess vascular structures due to artifacts. Patients over 50 years old were excluded from the study due to concerns regarding age-related vascular changes and confounding comorbidities. Pathological cases that would make it difficult to evaluate vascular structures and variations were excluded. In each case, the normal anatomy of the circle of Willis and its variations were evaluated and noted separately.

Magnetic Resonance Imaging Protocol

The study was performed with 1.5 T and 3T MR (Magnetom Skyra; Siemens Healthcare, Erlangen, Germany) devices. There was not exposure to radiation and no contrast material was used. The images on workstations that provide multi-planar imaging and noted the variations for each case were evaluated.

Magnetic Resonance Imaging Evaluation

Images were evaluated by 1 radiologist with 10 year experience in neuroradiology. Axial, coronal, sagittal images and multi-planar reconstructions were all evaluated together. The variations that were evaluated in the study are as follows: AComA aplasia, right and left ACA A1 aplasia-hypoplasia, ACA trifurcation (Figure 1), azygos ACA (Figure 2), bi-hemispheric ACA, right and left AComP aplasia-hypoplasia (Figure 3), right, left, and bilateral ACP fetal configuration,

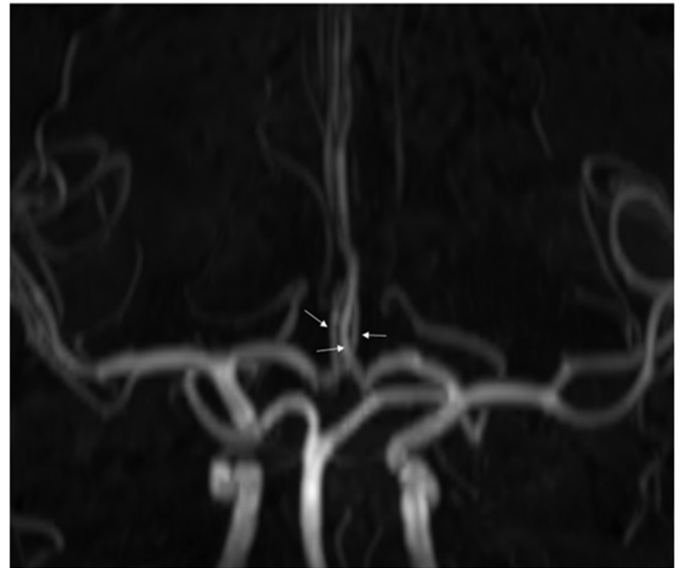


Figure 1. ACA trifurcation in A2 segment (thin arrows).

persistent trigeminal artery (PTA) (Figure 4), fenestration in BA, hypoplasia in right and left vertebral artery. Absence of an artery is diagnosed as aplasia and a diameter smaller than 1 mm as hypoplasia.

Statistical Analysis

Analyses were performed using the IBM SPSS 20 (IBM SPSS Corp.; Armonk, NY, USA) statistical analysis program. Shapiro–Wilk W test and Kolmogorov–Smirnov test were used to check the normal distribution of continuous variables. In comparisons between 2 independent groups consisting of male and female subjects, the Independent Samples *t* test was used when the normal distribution condition was met, and the Mann–Whitney *U* test was used when it was not met. In 2×2 comparisons between categorical variables (>5), the Pearson chi-square test was used, the chi-square Yates test was used for expected values (3–5), and Fisher's exact test was used for expected values (<3). Statistical significance level was taken as $P < .05$.

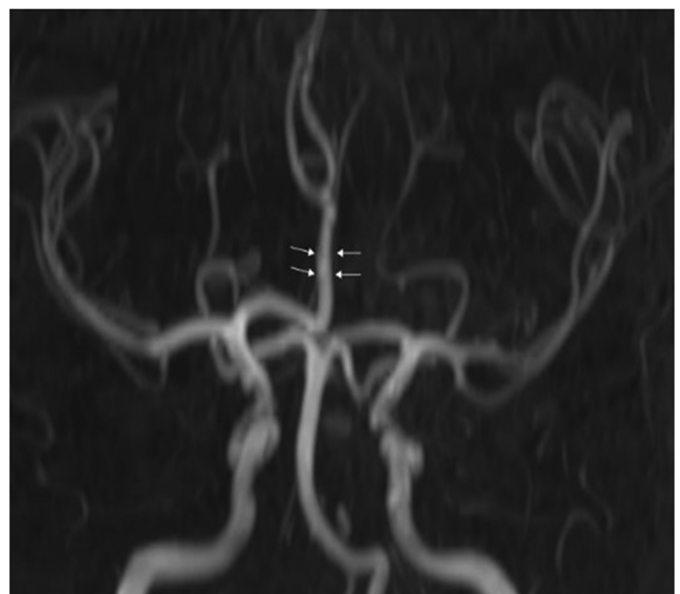


Figure 2. Azygos variation in ACA A2 segment (thin arrows).

MAIN POINTS

- Two hundred fifty patients without specific neurological symptoms were evaluated to determine circle of Willis variations in the Eastern Anatolia region.
- The typical polygonal structure where all the arteries are located was detected at a rate of 32%.
- Willis polygon variations were more frequent in the posterior part of the polygon, consistent with the literature.
- The most frequently detected variations were aplasia/hypoplasia, with the most frequently detected was arteria communicans posterior (between 10% and 16.8%).
- The most frequently detected variation in anterior circulation was arteria cerebri anterior trifurcation (7.6%), and it was similar to the literature.

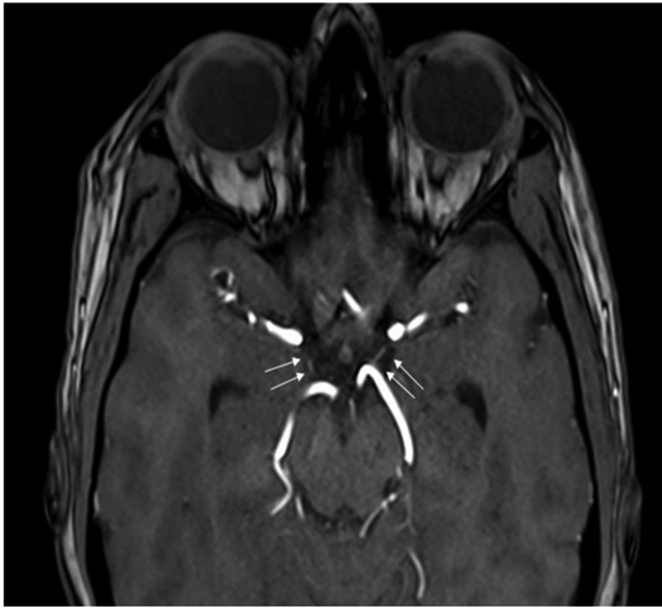


Figure 3. Bilateral hypoplasia of arteria communicans posterior.

RESULTS

Patient Demographics

Study group consisted of 250 patients, 95 were male (38%) and 155 were female (62%). The age range was 18-50 for both genders, and the mean age was 36 for males and 35.8 for females.

The typical (complete-normal) polygonal structure in which all arteries forming the circle of Willis were present was observed in a total of 80 cases (32%). The number and rates of variations in the study group are summarized in Table 1; the distribution of variations by gender is summarized in Table 2.

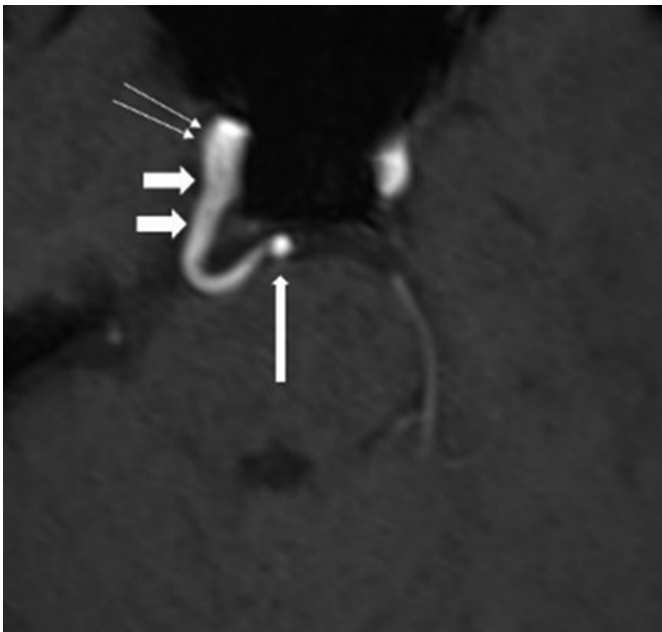


Figure 4. Persistent trigeminal artery between the right internal carotid artery (ICA) and the basilar (ICA - thin arrows, basilar artery - long arrow, and persistent trigeminal artery - short thick arrows).

Table 1. Number and Percentages of Variations in Circle of Willis

	Number	Percentage (%)
A Com A Ap	1	4
R ACA A1 Ap	1	11
L ACA A1 Ap	1	5
R ACA A1 Hp	1	14
L ACA A1 Hp	1	6
ACA Trifurcation	1	19
Azygos ACA	1	2
Bi-hemispheric ACA	1	4
R A Com P Ap	1	42
L A Com P Ap	1	32
R A Com P Hp	1	25
L A Com P Hp	1	26
Fetal RPCA	1	26
Fetal LPCA	1	15
Fetal BPCA	1	16
BA fenestration	1	3
R VA V4 Hp	1	20
L VA V4 Hp	1	14
PTA	1	3

A Com A Ap, Arteria Communicans Anterior Aplasia; ACA, Anterior Cerebral Artery; BA, basilar artery; BPCA, bilateral Posterior Cerebral Artery; Hp, hypoplasia; L A Com P Ap, left Arteria Communicans Posterior Aplasia; L A Com P Hp, left Arteria Communicans Posterior Hypoplasia; L ACA A1 Ap, left Anterior Cerebral Artery A1 Aplasia; L ACA A1 Hp, left Anterior Cerebral Artery A1 hypoplasia; LPCA, left Posterior Cerebral Artery; PTA, persistent trigeminal artery; R A Com P Ap, right Arteria Communicans Posterior Aplasia; R A Com P Hp, right Arteria Communicans Posterior Hypoplasia; R ACA A1 Ap, right Anterior Cerebral Artery A1 Aplasia; R ACA A1 Hp, right Anterior Cerebral Artery A1 Hypoplasia; RPCA, right Posterior Cerebral Artery; VA, vertebral artery.

AComA aplasia was detected in a total of 4 cases (1.62%). Right ACA A1 segment aplasia and left ACA A1 segment aplasia were detected in numbers and ratios of 11 (4.4%) and 5 (2%), respectively. Right ACA A1 segment hypoplasia and left ACA A1 segment hypoplasia were detected in 14 (5.5%) and 6 (2.4%) numbers and rates, respectively. There are 3 A2 segments in the ACA trifurcation, also called the persistent medial callosal artery. The number of cases in which ACA trifurcation was detected is 19 (7.6%). While the most common variation in the anterior circulation was ACA trifurcation (7.6%), the least common variation was azygos ACA variation. A single A2 is observed in azygos ACA variation. In general, the majority of the variations that were detected belonged to the posterior circulation. The most common variations that were detected were aplasia and hypoplasia. The localization in which aplasia and hypoplasia were detected most frequently is AComP. The variations detected in the posterior circulation and their numbers are as follows: Right AComP aplasia and left AComP aplasia were detected in the numbers and ratios of 42 (16.8%) and 32 (12.8%), respectively.

Variations of the fetal ACP configuration constitute the second most frequently detected variation group after aplasia and hypoplasia. These variations were determined according to the relationship between the AComP and ACP P1 segment diameters; cases where the AComP diameter is larger than the ACP P1 segment are called fetal configuration. In this study, the fetal configuration of the ACP was grouped as right, left, and bilateral. In this group, the right fetal configuration was determined as 26 (10.4%), the left fetal configuration as 15 (6%), and the bilateral fetal configuration as 16 (6.4%). The term fenestration refers to the appearance of the vascular structure ending with the division of its lumen into 2 sections, each with its own endothelial layer, running parallel to each other and then reuniting. In this

Table 2. Distribution of Variations According to Genders

		Gender				Chi-Square	P
		M		F			
		Number	Percentage (%)	Number	Percentage (%)		
A Com A Ap	1	2	2.1	2	1.3		.64
R ACA A1 Ap	1	6	6.3	5	3.2	0.69	.41
L ACA A1 Ap	1	2	2.1	3	1.9		1
R ACA A1 Hp	1	7	7.4	7	4.5	0.88	.35
L ACA A1 Hp	1	2	2.1	4	2.6		1
ACA Trifurcation	1	7	7.4	12	7.8	0.02	.90
Azygos ACA	1	2	2.1	0	0.0		.15
Bi-hemispheric ACA	1	3	3.2	1	0.6		.16
R A Com P Ap	1	20	21.1	22	14.3	1.92	.17
L Com P Ap	1	11	11.6	21	13.6	0.22	.64
R Com P Hp	1	8	8.4	17	11.0	0.45	.50
L Com P Hp	1	8	8.4	18	11.7	0.67	.41
Fetal RPCA	1	10	10.5	16	10.4	0.001	.97
Fetal LPCA	1	5	5.3	10	6.5	0.16	.69
Fetal BPCA	1	5	5.3	11	7.1	0.35	.56
BA fenestration	1	0	0.0	3	1.9		.29
PTA	1	1	1.05	2	1.3		.29
R VA V4 Hp	1	7	7.4	13	8.4	0.092	.76
L VA V4 Hp	1	7	7.4	7	4.5	0.882	.35

A Com A Ap, Arteria Communicans Anterior Aplasia; ACA, Anterior Cerebral Artery; BA, basilar artery; BPCA, bilateral Posterior Cerebral Artery; Hp, hypoplasia; L A Com P Ap, left Arteria Communicans Posterior Aplasia; L A Com P Hp, left Arteria Communicans Posterior Hypoplasia; L ACA A1 Ap, left Anterior Cerebral Artery A1 Aplasia; L ACA A1 Hp, left Anterior Cerebral Artery A1 hypoplasia; LPCA, left Posterior Cerebral Artery; PTA, persistent trigeminal artery; R A Com P Ap, right Arteria Communicans Posterior Aplasia; R A Com P Hp, right Arteria Communicans Posterior Hypoplasia; R ACA A1 Ap, right Anterior Cerebral Artery A1 Aplasia; R ACA A1 Hp, right Anterior Cerebral Artery A1 Hypoplasia; RPCA, right Posterior Cerebral Artery; VA, vertebral artery.

study group, fenestration was detected in the BA in 3 cases (1.2%). The number and rates of cases in which the authors detected right and left vertebral artery V4 segment hypoplasia are 20 (8%) and 14 (5.6%), respectively.

Although PTA variation is rare in the population, it is the most common variation among persistent carotid-BA variations. Persistent trigeminal artery variation was detected in a total of 3 cases (1.2%) in this study group.

There is not any statistically significant difference between age and gender in terms of the frequency and localization of variations.

DISCUSSION

Various variations of the Willis polygon have been defined in the literature, and the names, numbers, criteria, and diversity of the variations included in the studies vary. This is the main reason for the significant difference in the rate of variation among studies. In addition, it is seen that there is no consensus on the definition of hypoplasia, and the cut-off value for hypoplasia is taken as 0.5 mm, 0.8 mm, or 1 mm in different studies.^{3,7,8}

Variations of the circle of Willis are more frequently seen in the posterior part of the circle. The most common localization has been reported as AComP in a cadaver study by Karataş et al.⁹ In another study by Karataş et al.⁹ examined variations of aplasia, hypoplasia, and fetal ACP in their 100-case study with CTA, and accepted the hypoplasia criterion as 1 mm, and found a variation rate of 72%, and the most common variation was AComP hypoplasia with a rate of 22%.¹⁰ In this study, variations were more frequent in the posterior part of the circle, in line with the literature. The most frequently detected variations were AComP aplasia and hypoplasia. Right AComP aplasia was 16.8% and

left AComP aplasia was 12.8%; right AComP hypoplasia was 10% and left AComP hypoplasia was 10.4%.

In a study conducted on 1205 cases with CTA, a total of 21 variations were examined, the hypoplasia limit was accepted as 1 mm, variation was detected in 95.4% of the cases, and the most frequently detected variation was reported as AComP hypoplasia, detected at a rate of 32%.¹¹ In cerebral aneurysm treatments and carotid ligation, accurate determination of the polygon structure and variations is very important in terms of determining adequate cerebral circulation. Variations of the Willis polygon are frequently seen, but they usually do not cause serious clinical consequences. However, it should not be forgotten that the presence of hypoplasia or aplasia of AComP in internal carotid artery occlusions is an independent risk factor for cerebral infarction. Therefore, unilateral ligation of the ACI in such a case can cause very important clinical problems.

Leptomeningeal collaterals cannot form in fetal variant of circle of Willis since both MCA and PCA are connected to ICAs. Thus there is an increased risk for stroke in patients with fetal PCA variant with obstructive arterial disease.¹² In AComP aneurysms, in the presence of fetal ACP configuration; AComP should be protected. Variations may develop outside the normal polygonal structure. However, it is not known exactly why and when these variations develop. Padgett defined 3 configurations according to AComP and ACP diameters.¹³ The type called adult configuration represents the situation where the diameter of AComP is smaller than the P1 segment of ACP. Adult configuration was found to be 87% in a study performed on 100 cadavers by Karataş et al.⁹ The adult configuration was detected at a rate of 72% in the study. In the second type called fetal configuration; the diameter of AComP is larger than the P1 segment of ACP. Therefore, the vascularization of the occipital lobe is largely provided by the internal carotid

artery. The frequency of this configuration in adults was reported in 9% by Karataş et al.⁹ In this study group, frequency of fetal configuration was 0.4% for right fetal configuration, 6% for left fetal configuration, and 6.4% for bilateral fetal configuration. Transitional configuration, in which the diameter of AComP and P1 are equal, was found in 5.2%.

The term fenestration refers to the appearance of the vascular structure during its course, when its lumen divides into 2 sections, each with its own endothelial layer, and runs parallel to each other, and then reunites. Data on the incidence of BA fenestration vary in the literature. It has been found to be 0.28%-5.26% in autopsy series, 0.3%-0.6% in studies conducted with angiography, and 1.0%-2.7% in MRA series.¹⁴ In this study group, BA fenestration was found to be present in 1.2% of patients, similar to MRA series. Persistent carotid-basilar anastomoses are rare variations. Among these, the most common is the PTA variation seen between the ICA cavernous segment and the BA, with a rate of 83%. Its incidence is between 0.1% and 0.6% in cerebral angiographies. It is mostly seen unilaterally. The PTA regresses after the development of AComP. It is important to know this variation, especially in cases of trans-sphenoidal surgery. In this study, PTA variation was detected in 3 cases (1.2%).

Variations in the anterior section of the polygon are less frequently detected than in the posterior section, but are important in terms of pathologies such as aneurysms that may accompany. ACA A1 segment aplasia is a rare variation and has been observed at rates ranging from 0.3% to 2% in anatomic studies and 0.7% to 2% in angiographic series.¹⁵ In this study, right ACA A1 aplasia was detected at a rate of 4.4% and left ACA A1 aplasia was detected at a rate of 2%. While ACA A1 segment hypoplasia is seen between 1% and 10% in the literature,¹⁶ right ACA A1 hypoplasia was detected at a rate of 5.5% and left ACA A1 hypoplasia was detected at a rate of 2.4% in this study. In another study conducted with CTA, A1 segment aplasia was reported at a rate of 6% and A1 segment hypoplasia at a rate of 1%. In the same study, it was emphasized that the rate of A1 aplasia was detected at a higher rate than in the literature and AComA aneurysm was observed in 16% of the cases.¹¹ In a study by Kapoor et al,¹⁷ A1 segment aplasia was found to be 0.4% and hypoplasia was detected in 1.7%. Both A1 aplasia and hypoplasia was detected at a higher rate in this study. The difference between results among different studies may be related to genetic, environmental, or combination of these factors and these factors should be further investigated. Another variation related to the anterior circulation in the literature is ACA trifurcation, which was reported at a rate of 8%.¹⁰ In this study, a similar rate of ACA trifurcation variation was detected (7.6%).

Variations are common, but most of them do not pose a serious problem in the clinic. Again, the recovery levels of patients in occlusive vascular diseases can be explained by variations in the Willis polygon. The fact that various branches of the polygon are too thin to function or are completely absent is very important in occlusive vascular diseases and cerebrovascular surgery. In patients undergoing surgical intervention, anatomical determination of the normal structure and variations of the Willis polygon with TOF MRA, which is a non-invasive imaging method that does not require radiation exposure or contrast material, will help reduce the significant neurological complications that may arise and the associated morbidity and mortality risk. However, MRA has disadvantages such as being sensitive to motion artifacts and application limitations in patients with devices such as pacemakers, neurostimulators, and infusion pumps. Again, it should be kept in mind that hypoplasia or aplasia diagnoses may not be sufficiently reliable due to

technical difficulties in evaluating arteries with diameters smaller than 1 mm in TOF MRA examination.

In conclusion, TOF MRA can be used to evaluate cerebral vascular anatomy, especially for screening and pre-surgical evaluation of asymptomatic or normal individuals. In cerebrovascular interventions, knowing anatomical variations and demonstrating the anomaly in advance is important for safe surgical intervention. Although TOF MRA can be used to examine circle of Willis without radiation exposure and the need for contrast material; technical difficulties in imaging some vessels, MRA's sensitivity to motion artifacts, and some application limitations such as pacemakers should be considered as disadvantages of the method.

Data Availability Statement: The data that support the findings of this study are available on request from the corresponding author.

Ethics Committee Approval: Ethics committee approval was received for this study from the ethics committee of Atatürk University (Approval No: B.30.2.ATA.0.01.00/277; Date: 30.05.2019).

Informed Consent: Written informed consent was obtained from patients who agreed to take part in the study.

Peer-review: Externally peer-reviewed.

Author Contributions: Concept – F.G.; Design – F.G.; Supervision – İ.M.; Resources – F.G.; Materials – A.T.A.; Data Collection and/or Processing – F.G.; Analysis and/or Interpretation – F.G.; Literature Search – F.G.; Writing Manuscript – A.T.A.; Critical Review – İ.M.

Declaration of Interests: The authors have no conflict of interest to declare.

Funding: The authors declared that this study has received no financial support.

REFERENCES

1. Rosner J, et al. Neuroanatomy, circle of Willis. *StatPearls*. 2025.
2. Grand W. The anatomy of the brain, by Thomas Willis. *Neurosurgery*. 1999;45(5):1234-6; discussion 1236. [\[CrossRef\]](#)
3. Rhoton AL, Jr. The supratentorial arteries. *Neurosurgery*. 2002;51(4)(suppl):S53-S120.
4. Rengachary SS, Xavier A, Manjila S, et al. The legendary contributions of Thomas Willis (1621-1675): the arterial circle and beyond. *J Neurosurg*. 2008;109(4):765-775. [\[CrossRef\]](#)
5. Hamming AM, van Walderveen MAA, Mulder IA, et al. Circle of Willis variations in migraine patients with ischemic stroke. *Brain Behav*. 2019;9(3):e01223. [\[CrossRef\]](#)
6. van Seeters T, Hendrikse J, Biessels GJ, et al. Completeness of the circle of Willis and risk of ischemic stroke in patients without cerebrovascular disease. *Neuroradiology*. 2015;57(12):1247-1251. [\[CrossRef\]](#)
7. Krabbe-Hartkamp MJ, van der Grond J, de Leeuw FE, et al. Circle of Willis: morphologic variation on three-dimensional time-of-flight MR angiograms. *Radiology*. 1998;207(1):103-111. [\[CrossRef\]](#)
8. Riggs HE, Rupp C. Variation in form of circle of Willis. The relation of the variations to collateral circulation: anatomic analysis. *Arch Neurol*. 1963;8:8-14. [\[CrossRef\]](#)
9. Karatas A, Yilmaz H, Coban G, Koker M, Uz A. The anatomy of Circulus arteriosus cerebri (circle of Willis): A study in Turkish population. *Turk Neurosurg*. 2016;26(1):54-61. [\[CrossRef\]](#)
10. Karatas A, Coban G, Cinar C, Oran I, Uz A. Assessment of the circle of Willis with cranial tomography angiography. *Med Sci Monit*. 2015;21:2647-2652. [\[CrossRef\]](#)
11. Kahraman F, İntraserebral WPV. Multiple Anevrizmalarla Olan ilişkisi. *Relat Between Var Circle Willis Mult Intracerebral Aneurysms*. 2020.
12. van Raamt AF, Mali WPTM, van Laar PJ, van der Graaf Y. The fetal variant of the circle of Willis and its influence on the cerebral collateral circulation. *Cerebrovasc Dis*. 2006;22(4):217-224. [\[CrossRef\]](#)
13. DH P. Intracranial arterial aneurysms. In: DH P, ed. *The circle of Willis Its embryology and anatomy*; 1944:67-90.

14. Sogawa K, Kikuchi Y, Ouchi T, Tanaka M, Inoue T. Fenestrations of the basilar artery demonstrated on magnetic resonance angiograms: an analysis of 212 cases. *Interv Neuroradiol.* 2013;19(4):461-465. [\[CrossRef\]](#)
15. Şahin H, Pekçevik Y. Anatomical variations of the circle of Willis: evaluation with CT angiography. *Anatomy.* 2018;12(1):20-26. [\[CrossRef\]](#)
16. Mäurer J, Mäurer E, Perneczky A. Surgically verified variations in the A1 segment of the anterior cerebral artery. Report of two cases. *J Neurosurg.* 1991;75(6):950-953. [\[CrossRef\]](#)
17. Kapoor K, Singh B, Dewan LJ. Variations in the configuration of the circle of Willis. *Anat Sci Int.* 2008;83(2):96-106. [\[CrossRef\]](#)

The Diffusion Tensor Imaging Features in the Visual Pathways of Patients with Cavernous Sinus Meningioma Treated by Gamma Knife Radiosurgery

Hafize Otçu Temur¹, Alpay Alkan¹, Mustafa Aziz Hatiboğlu², İsmail Yurtsever¹, Kerime Akdur², Özlem Toluk³, Mehmet Hakan Seyithanoğlu²

¹Department of Radiology, Bezmialem Vakıf University Faculty of Medicine, İstanbul, Türkiye

²Department of Neurosurgery, Bezmialem Vakıf University Faculty of Medicine, İstanbul, Türkiye

³Department of Biostatistics, Bezmialem Vakıf University Faculty of Medicine, İstanbul, Türkiye

Cite this article as: Otçu Temur H, Alkan A, Hatiboğlu MA, et al. The diffusion tensor imaging features in the visual pathways of patients with cavernous sinus meningioma treated by gamma knife radiosurgery. *Current Research in MRI*, 2025;4(1):7-11.

Corresponding author: Hafize Otçu Temur, e-mail: hotcutemur@bezmialem.edu.tr

Received: March 27, 2025 **Revision Requested:** April 24, 2025 **Last Revision Received:** May 28, 2025 **Accepted:** June 17, 2025 **Publication Date:** August 22, 2025

DOI: 10.5152/CurrResMRI.2025.25113



Content of this journal is licensed under a Creative Commons Attribution-NonCommercial 4.0 International License.

Abstract

Objective: The objectives of this study are to evaluate the effects of diffusion tensor imaging (DTI) on visual pathways following Gamma Knife radiosurgery (GKR) and to identify any correlations between DTI results and radiosurgery data.

Methods: Thirteen patients with cavernous sinus meningiomas (CSMs) and 15 controls were included. Mean diffusion coefficient (ADC), fractional anisotropy (FA), and radial diffusivity (RD) were assessed in the visual pathways using DTI, and DTI values were compared between healthy subjects and patients before and after 12 months of GCR imaging. Additionally, the correlation between these values and radiosurgery data was also investigated.

Results: The ADC, FA, and RD values measured at visual pathways prior to and following GKR did not differ statistically. The FA values obtained from optic chiasm and occipital lobe were negatively correlated with the maximum and mean radiation dose to the prechiasmatic optic nerve and optic apparatus, respectively. The maximum radiation dose to the optic apparatus and the RD values obtained from the optic chiasm were found to be positively correlated. The maximum and mean radiation doses to the optic apparatus were found to positively correlate with the ADC and RD values obtained from the occipital lobe.

Conclusion: Defining the radiation-related microstructural diffusion changes in visual pathways following GKR may provide useful information for tailoring the radiosurgical approach and safety of the treatment. Diffusion tensor imaging may provide useful information to characterize changes of the radiation effects on visual pathways in patients with CSMs after GKR.

Keywords: Cavernous sinus meningioma, diffusion tensor imaging, magnetic resonance imaging, optic chiasm, visual pathways

INTRODUCTION

The prevalence of cavernous sinus meningiomas (CSMs) in the general population is 0.5 per 100 000.¹ The risk of meningiomas is increased by advanced age and female sex. Meningiomas are mostly benign, well-defined, and low-proliferating tumors.² It is possible to classify CSMs according to their anatomic localization. They may originate from the clinoid processes or dura of the cavernous sinus (CS), the sphenoid ridge dura, or the petroclival area that extends to or penetrates the CS.³ The most common presenting symptoms of meningiomas are ocular motor deficits, diplopia, ptosis, anisocoria, or complete ophthalmoplegia. The optic nerve compression by the tumor can cause visual field deficits, and carotid artery compression can cause ischemic deficits.⁴

CSMs usually cannot be completely resected because they are closely related to multiple critical structures, including the cerebral artery, optic nerves, ocular motor nerves, and pituitary body. Cavernous sinus meningiomas can be treated with systemic medicine, Gamma Knife Radiosurgery (GKR), surgical resection, attentive observation, or a combination of these various methods.^{2,3}

A magnetic resonance imaging (MRI) method called diffusion tensor imaging (DTI) is used to evaluate the microstructural changes in the white matter. The DTI evaluates visual pathways by measuring the changes in average diffusion coefficient (ADC), fractional anisotropy (FA), and radial diffusivity (RD) values of the visual pathways. Evaluation of FA provides information on the structural integrity of the fiber tracts, axonal degeneration, and structural irregularity while RD shows de/dysmyelination of white matter and changes in the axonal diameters or density.^{5,6} Previous DTI studies have found that reduced FA values are associated with visual impairment in a variety of diseases, such as Alzheimer's disease, moderate cognitive impairment, and glaucoma.⁷⁻²³

As far as the authors are aware, no research has been done in the literature to assess how radiation affects visual pathways in patients receiving GKR for meningiomas using the DTI approach. This study's objectives were to determine whether DTI altered visual pathways following GKR and to identify a connection between DTI and radiosurgery parameters in CSM patients.

MATERIAL AND METHODS

Thirteen patients (2 men, 11 women, median age 51 years; range: 31-81 years) with CSMs and 15 healthy controls (3 men, 12 women, median age 44 years; range: 32-57 years) were enrolled. Patients having conditions that can significantly affect DTI parameters, including as strokes, microhemorrhages, small-vessel disorders, and demyelination, were not included. 2 of patients had undergone operation because of CSM before GKR. The other patients treated by GKR first. The institutional ethics committee has accepted the study, which is a retrospective (decision dated March 13, 2018, numbered 6/70). The individuals who consented to participate in the study provided written informed consent. Radiosurgical variables including marginal dose, the mean and maximum dose receiving optic apparatus (including prechiasmatic segment of optic nerve and chiasm) were retrospectively reviewed. Then the doses received by the optic chiasm and prechiasmatic segment of optic nerve were calculated separately. Magnetic resonance imaging and DTI performed all cases before and 12 months after GKR. The ipsilateral and contralateral sides of the optic chiasm (Figure 1) and the subcortical white matter at the level of calcarine cortex in the occipital lobe (Figure 2) were used to measure the ADC, FA, and RD values. Average DTI values were found along the left side of the visual pathway in the control group. Computerized static perimetry performed to evaluate visual field before and 12 months after GKR. The MD (mean deviation), PSD (pattern SD) values were measured.

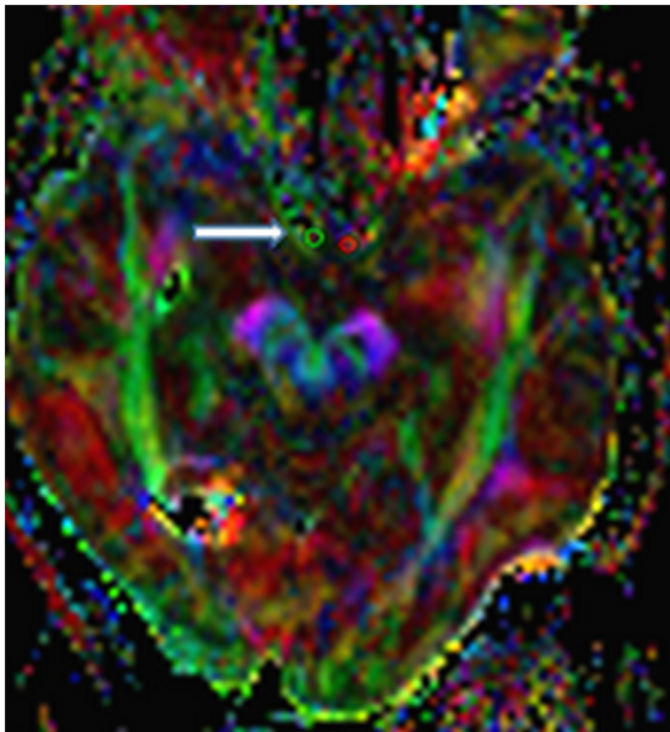


Figure 1. The axial color-coded maps shows the region of interests placed on the ipsilateral and contralateral optic chiasm (long arrow).

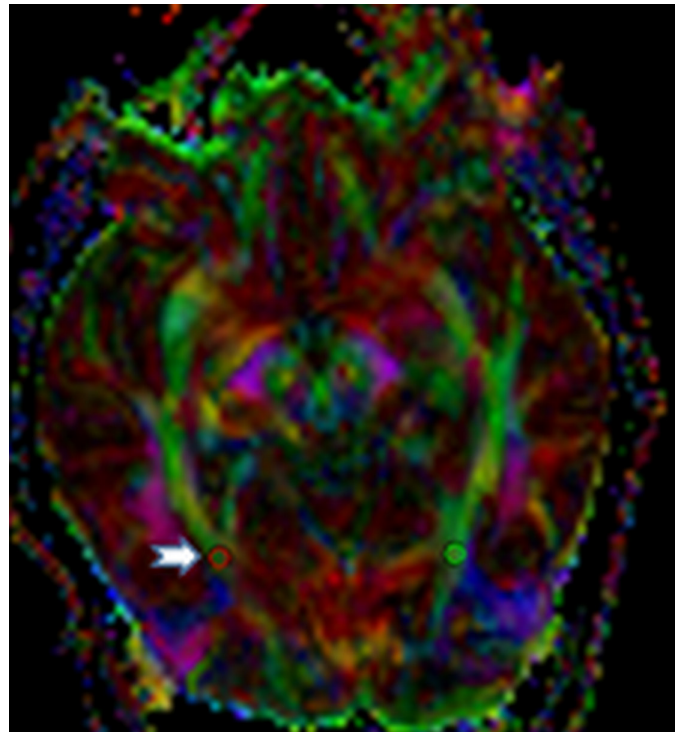


Figure 2. The axial color-coded maps shows the region of interests placed on the ipsilateral and contralateral occipital lobe (short arrow).

MRI Protocol: 1.5T MRI (Siemens, Avanto, Erlangen, Germany) was used with a head coil. T1-weighted (T1-W) spin echo (TR/TE, 460/14 ms), T1W with fat suppression (TR/TE, 715/7.5 ms) with and without contrast medium (gadolinium diethylenetriamine pentaacetic acid, 0.1 mmol/kg body weight, intravenously), T2-weighted (T2-W) turbo spin echo (TR/TE, 2500/80 ms), FLAIR (TR/TE, 8000/90 ms), T1-W spin echo (TR/TE, 460/14 ms) were obtained for brain MRI. With an isotropic voxel resolution of 1 mm, a magnetization-prepared rapid acquisition of gradient echo sequence was used to add the 3D T1-W volumetric sequences (TR/TE/TI, 12.5/5/450 ms) with and without contrast. An integrated parallel acquisition technique (iPAT) factor of 2 was used in conjunction with generalized autocalibrating partially parallel acquisition (GRAPPA) for parallel imaging. The DTI images obtained in the axial plane comprised a single-shot, spin echo, echo-planar sequence with TR/TE, 2700/89 ms; matrix, 128 × 128; field of view, 230 mm; slice thickness 5 mm; and 30 diffusion-encoding directions were used at $b = 1000 \text{ s/mm}^2$ and $b = 0 \text{ s/mm}^2$. Generalized autocalibrating partially parallel acquisition with an iPAT factor of 3 was used for parallel imaging. The Leonardo console (software version 2.0; Siemens) was used to rebuild the ADC, FA, and RD maps. The areas of interest (ROIs) were positioned and traced using the 3D T1-W and T2-W images as anatomical references. At the same section level, these images were combined with the matching area of the ADC and FA maps. At the level of the calcarine sulcus, each ROI was manually drawn with a size of 3 pixels at the chiasm and 4 pixels at the subcortical white matter of the occipital lobe. The ROIs' sizes and positions were adjusted by 2 experienced radiologists, who also evaluated them simultaneously on axial color-encoded FA maps based on "Dissecting the White Matter Tracts: An Interactive Instructional Atlas for Diffusion Tensor imaging." To avoid averaging artifacts and reduce the partial-volume effect, the slices above and below the region were compared side by side during ROI insertion

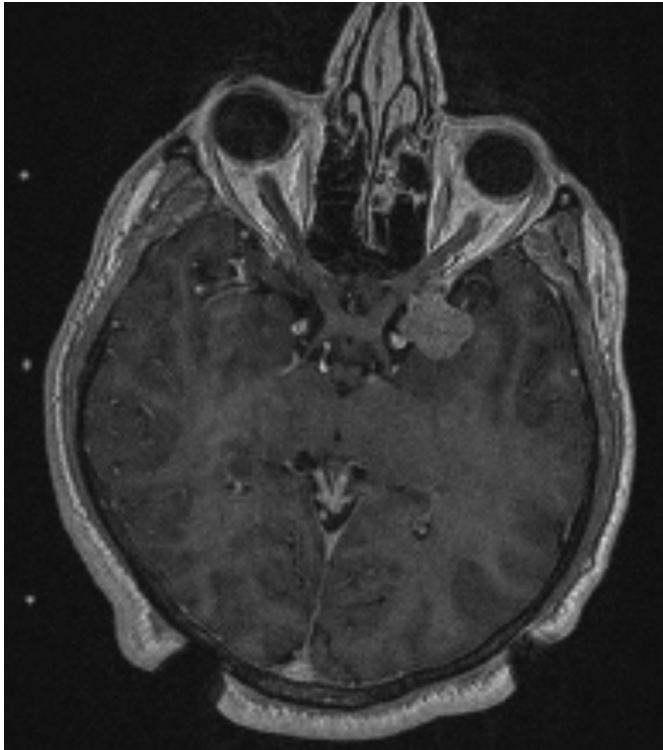


Figure 3. The axial 3D T1-weighted image, which used as an anatomic reference for treatment planning, shows the tumor and bilateral prechiasmatic parts of the optic nerves contoured to calculate the radiation dose received.

with the conventional images and color ADC, FA map, and diffusion trace.

Gamma Knife Protocol: The treatment was performed at the Gamma Knife Unit (Gamma Knife 4C model) of the university. After administering local anesthetic and placing a Leksell stereotactic head frame on the patient's head, MRI imaging was performed. The MRI data (T1W, T2W 3D images in the axial section) were transferred to the Gamma Plan version 10.1.1 software (Elekta AB, Stockholm, Sweden). The tumor and optic apparatus were contoured to plan treatment and perform dose calculations (Figure 3). The doses received by the optical apparatus were computed using the definition of the prescription dose. It is possible to modify the prescription dosage when certain factors surpass critical dose values. Every patient received a 50% isodose: the

median maximum optic apparatus dose was 8 Gy (range: 1-12 Gy) and median mean dose was 2.8 Gy (range: 1-5.7 Gy); the median treatment dose was 12 Gy (range: 10-14 Gy). No new neurological deficits were detected in any patients at 12 months after GKR.

Statistical Analysis

IBM SPSS 19.0 (IBM SPSS Corp.; Armonk, NY, USA) was used to analyze all of the data. ADC, FA, and RD values obtained from the visual pathways prior to and following GKR in the patients with CSMs and the control group were compared using ANOVA. To ascertain the connections among DTI results, radiosurgical treatment parameters, and visual field characteristics, the Tukey post hoc test was utilized. A type-1 error rate of $\alpha=0.05$ was used.

RESULTS

No statistical differences were observed in ADC, FA, and RD values measured from bilateral visual pathways prior to and following GKR in patients with CSM. There was no statistical difference in ADC, FA, and RD values measured in the control group and bilateral visual pathways before and after GKR in patients with CSM (Table 1).

The FA values obtained from optic chiasm were negatively correlated with the maximum and mean radiation dose to the prechiasmatic optic nerve (respectively, $r = -0.510$, $P = .011$, mean $r = -0.527$, $P = .008$). The maximum and mean radiation doses to the optic apparatus were negatively correlated with the FA measured from the occipital lobe (respectively, $r = -0.432$, $P = .035$, mean $r = -0.420$, $P = .04$).

The RD values obtained from optic chiasm were positively correlated with the maximum radiation dose to the prechiasmatic optic nerve and apparatus (respectively, $r = 0.429$, $P = .036$, $r = 0.406$, $P = .049$). There was a positive correlation between ADC and RD values measured from the occipital lobe and the mean radiation dose to the optic apparatus ($P < .05$).

Visual field tests and ophthalmological examinations were performed on all patients before and after GKR and in the control group. Patients with normal ophthalmological and fundus examinations and visual field tests were included in the control group. However, the results of 7 patients were obtained retrospectively. In these 7 patients, there was no statistical difference between MD and PSD values before and 12 months after GKR. There were no statistical differences between MD and PSD values before and 12 months after GKR, and there was no correlation between MD, PSA values, and DTI values (FA, ADC, RD)

Table 1. The Fractional Anisotropy, Average Diffusion Coefficient, and Radial Diffusivity Values Measured Before and After Gamma Knife Radiosurgery from Ipsilateral and Contralateral Sides in the Patients with Cavernous Sinus Meningioma and the Control Group

	Optic Chiasm			Occipital Lobe		
	FA	ADC	RD	FA	ADC	RD
Before GKR						
Ipsilateral side-before GKR	285 ± 89	1786 ± 547	1541 ± 532	331 ± 88	771 ± 74	644 ± 137
Contralateral side-before GKR	287 ± 117	1673 ± 314	1415 ± 314	361 ± 49	775 ± 78	653 ± 62
Control group	324 ± 97	1657 ± 480	1501 ± 540	339 ± 39	752 ± 53	613 ± 48
After GKR						
Ipsilateral side-after GKR	256 ± 65	2083 ± 802	1758 ± 582	319 ± 88	806 ± 102	666 ± 98
Contralateral side-after GKR	298 ± 44	1816 ± 470	1589 ± 671	326 ± 64	798 ± 105	653 ± 93
Control group	324 ± 97	1657 ± 480	1501 ± 540	339 ± 39	752 ± 53	613 ± 48
<i>P</i>	.35	.27	.57	.56	.45	.61

Data are presented as mean ± standard deviation ADC, apparent diffusion coefficient; FA, fractional anisotropy; RD, radial diffusivity; GKR, Gamma Knife radiosurgery. *P* values shows statistically not significant results

obtained at the optic chiasm and subcortical white matter of the occipital lobe obtained 12 months after GKR.

DISCUSSION

The optic strut separates the CS from the afferent visual pathway anteriorly, and the subarachnoid matter separates the optic nerve from the roof of the CS posteriorly. Nevertheless, the tumors that involve the CS can extend superiorly and affect the optic nerve or chiasm.²⁴ Recent studies have clearly indicated that curative surgery of CSMs alone is not a secure and sufficient treatment option in many cases. According to published research, surgery is linked to significant morbidity (17.9%–74%) and mortality (0%–9.5%) due to pituitary insufficiency, vascular damage, and cranial nerve abnormalities.^{25,26}

GKR is a reasonable, effective, and safe option for the primary or adjunctive treatment of these tumors. Radiosurgery has been widely used widely for treating benign tumors of the central nervous system. The most tumors that have been treated with GKR are acoustic neuromas and meningiomas of the skull base. It is important to preserve the neurological functions of the patients because meningiomas are benign lesions. Gamma Knife radiosurgery provides long-term overall tumor control and has extremely low morbidity rates.²⁷⁻²⁹ However, the optic apparatus is at risk of radiation toxicity.

Diffusion tensor imaging is a technique that determines the microstructural changes within the white matter by using diffusion measurements. Each DTI value (FA, ADC, and RD) is responsive to various aspects of white matter disease, such as neuronal damage, axonal degeneration, and maturation. Fractional anisotropy is very sensitive to changes in microstructure but less sensitive to changes of a particular kind (such as axial or RD). However, DTI is a potentially effective method for tracking how the brain reacts to treatments.⁵ Decreased FA and increased MD in the optic nerve are linked to progressive optic neuropathy, according to recent studies on glaucoma, amblyopia, retinitis pigmentosa, optic neuritis, and multiple sclerosis.¹⁵⁻²⁰ Nishioka et al²¹ reported that the visual pathway is impacted as Alzheimer's disease (AD) and moderate cognitive impairment (MCI) progress. In AD and MCI, there was an increase in RD and a decrease in FA at the optic nerve and tract. According to their findings, visual impairments in AD patients may be caused by damage to the visual white matter tracts. Adhikari et al²² stated that there was a negative correlation between retinotopically defined ganglion cell inner plexiform thickness (GCIPL) and optic tract MD and AD. The thickness of the retinotopically defined retinal nerve fiber layer was inversely connected with FA.

Chang et al²³ reported that significant relationships between Heidelberg Retina Tomography (HRT) rim area and DTI parameters in glaucoma patients. They showed that as HRT rim area decreased, MD, RD increased, while FA decreased in optic nerves. The retinal nerve fiber layer (RNFL) contains unmyelinated axons. Increased axonal loss in the RNFL is implied by a smaller retinal rim area. The linked downstream tissue, like the optic nerve, may experience myelin disintegration as a result of axonal degeneration, which also suggests axonal injury or loss.

For patients receiving radiosurgery treatment for CSM, GKR characteristics such as the mean and maximum radiation dose to the optical apparatus are crucial. According to the literature, CSMs are often treated for GKR with a peripheral dose of 12-14 Gy. To reduce the dose to organs at risk below 10 Gy, the tumor's closeness to optic pathways may dictate a dose reduction to 12 Gy.³ The volume of the optic

apparatus that receives large dosages is correlated with the likelihood of vision impairment. Klinger et al²⁸ showed that patients who received less than 10 Gy to the optic apparatus and those who received a peak dosage of less than 25 Gy to the CS did not experience any visual problems. In this study, the median maximum optic apparatus was 8 Gy (range: 1-12 Gy), the median optic apparatus dose was 2.8 (range: 1-5.7 Gy) and median treatment dose was 12 Gy (range: 10-14 Gy). There was no complication associated with visual pathways 12 months after GKR at the level of these radiation doses. It was found that ADC, FA, and RD values obtained from visual pathways do not significantly differ before and after GKR. Despite no statistical significance, there exists a trend for decrease in FA values in patients with CSMs before GKR compared to healthy controls.

Radiation therapy decreases the FA of impacted white matter regions, according to several research. The total radiation dose appears to have an impact on this decrease in FA, which might be used to evaluate dose distribution. While demyelination has no effect on the axial diffusivity, it may enhance the RD.⁵ The FAs recorded at the optic chiasm decrease as the mean and maximum radiation doses administered to the optic nerve rise. The RDs recorded at the optic chiasm increase in proportion to the maximal radiation exposure to the optic nerve and optic apparatus. As the maximum and mean radiation dose administered to the optic apparatus increase, the FAs obtained from the occipital lobe decrease and the ADC, RDs measured at the occipital dose increase. Decreased FA values in the occipital lobe and optic chiasma may indicate axonal structural irregularity, demyelination, axonal degeneration, and white matter disintegration. These findings in the study defining that the radiation dose-related microstructural changes in visual pathways following GKR. The limitation of this study is a small number of patients were included. And no other tests such as visual acuity or optical coherence tomography were performed on the patient or control groups. Fundus examination was not performed on the patient group. The fact that the visual impairments present in the patients before GKR treatment were not revealed by clinical data may have affected the findings in the comparison of DTI results of the control group and patients who underwent GKR.

To the best of the authors' knowledge, this is the first study to demonstrate DTI features of the visual pathways in CSMs patients treated with GKR. These results suggest that GKR does not change significantly the DTI changes at visual pathways. Microstructural diffusion changes in optic pathway were correlated with the mean and maximum radiation doses receiving optic apparatus at 12 months. Diffusion tensor imaging may provide useful information to characterize changes of the radiation effects on visual pathways in patients with CS meningioma after GKR.

Data Availability Statement: The data that support the findings of this study are available on request from the corresponding author.

Ethics Committee Approval: This study was approved by the Ethics Committee of Bezmialem Vakıf University (Approval No: 6/70; Date: 13.03.2018).

Informed Consent: Written informed consent was obtained from participants who agreed to take part in the study.

Peer-review: Externally peer-reviewed.

Author Contributions: Concept – H.O.T., A.A.; Design – A.A.; Supervision – A.A., M.H.S.; Resources – H.O.T., K.A., İ.Y.; Materials – K.A., İ.Y.; Data Collection and/or Processing – M.A.H., M.H.S., K.A., İ.Y., Ö.T.; Analysis and/or Interpretation – M.A.H., H.O.T., Ö.T.; Literature Search – H.O.T., İ.Y.; Writing Manuscript - H.O.T.; Critical Review – A.A., M.A.H.

Declaration of Interests: Alpay Alkan is an Emergency Radiology Editor at Current Research in MRI; however his involvement in the peer-review process was solely as an author. The other authors have no conflict of interest to declare.

Funding: The authors declared that this study has received no financial support.

REFERENCES

- Perry A, Scheithauer BW, Stafford SL, Lohse CM, Wollan PC. "Malignancy" in meningiomas: a clinicopathologic study of 116 patients, with grading implications. *Cancer*. 1999;85(9):2046-2056. (doi:10.1002/(sici)1097-0142(19990501)85:9<2046::aid-cnrc23>3.0.co;2-m)
- Correa SFM, Marta GN, Teixeira MJ. Neurosymptomatic cavernous sinus meningioma: a 15 years experience with fractionated stereotactic radiotherapy and radiosurgery. *Radiat Oncol*. 2014;9:1.
- Fariselli L, Biroli A, Signorelli A, Broggi M, Marchetti M, Biroli F. The cavernous sinus meningiomas' dilemma: surgery or stereotactic radiosurgery? *Rep Pract Oncol Radiother*. 2016;21(4):379-385. [CrossRef]
- Heth JA, Al-Mefty O. Cavernous sinus meningiomas. *Neurosurg Focus*. 2003;14(6):e3. [CrossRef]
- Alexander AL, Lee JE, Lazar M, Field AS. Diffusion tensor imaging of the brain. *Neurotherapeutics*. 2007;4(3):316-329. [CrossRef]
- Hui ES, Fu Q, So K, Wu EX. Diffusion tensor MR study of optic nerve degeneration in glaucoma. In: *Proceedings of the 29th Annual International Conference of the IEEE EMBS*. New York: IEEE; 2007:4312-4315. [CrossRef]
- Sidek S, Ramli N, Rahmat K, Ramli NM, Abdulrahman F, Tan LK. Glaucoma severity affects diffusion tensor imaging (DTI) parameters of the optic nerve and optic radiation. *Eur J Radiol*. 2014;83(8):1437-1441. [CrossRef]
- Garaci FG, Bolacchi F, Cerulli A, et al. Optic nerve and optic radiation neurodegeneration in patients with glaucoma: in vivo analysis with 3-T diffusion-tensor MR imaging. *Radiology*. 2009;252(2):496-501. [CrossRef]
- Engelhorn T, Haider S, Michelson G, Doerfler A. A new semi-quantitative approach for analysing 3 T diffusion tensor imaging of optic fibres and its clinical evaluation in glaucoma. *Acad Radiol*. 2010;17(10):1313-1316. [CrossRef]
- Engelhorn T, Michelson G, Waerntges S, Struffert T, Haider S, Doerfler A. Diffusion tensor imaging detects rarefaction of optic radiation in glaucoma patients. *Acad Radiol*. 2011;18(6):764-769. [CrossRef]
- Engelhorn T, Michelson G, Waerntges S, et al. A new approach to assess intracranial white matter abnormalities in glaucoma patients: changes of fractional anisotropy detected by 3 T diffusion tensor imaging. *Acad Radiol*. 2012;19(4):485-488. [CrossRef]
- Nucci C, Mancino R, Martucci A, et al. 3-T diffusion tensor imaging of the optic nerve in subjects with glaucoma: correlation with GDx-VCC, HRT-III and Stratus optical coherence tomography findings. *Br J Ophthalmol*. 2012;96(7):976-980. [CrossRef]
- Michelson G, Engelhorn T, Waerntges S, El Rafei A, Hornegger J, Doerfler A. DTI parameters of axonal integrity and demyelination of the optic radiation correlate with glaucoma indices. *Graefes Arch Clin Exp Ophthalmol*. 2013;251(1):243-253. [CrossRef]
- Chen Z, Lin F, Wang J, et al. Diffusion tensor magnetic resonance imaging reveals visual pathway damage that correlates with clinical severity in glaucoma. *Clin Exp Ophthalmol*. 2013;41(1):43-49. [CrossRef]
- Allen B, Schmitt MA, Kushner BJ, Rokers B. Retinothalamic white matter abnormalities in amblyopia. *Invest Ophthalmol Vis Sci*. 2018;59(2):921-929. [CrossRef]
- Zhang QJ, Wang D, Bai ZL, Ren BC, Li XH. Diffusion tensor imaging of optic nerve and optic radiation in primary chronic angle-closure glaucoma using 3T magnetic resonance imaging. *Int J Ophthalmol*. 2015;8(5):975-979. [CrossRef]
- Wang MY, Wu K, Xu JM, et al. Quantitative 3-T diffusion tensor imaging in detecting optic nerve degeneration in patients with glaucoma: association with retinal nerve fiber layer thickness and clinical severity. *Neuro-radiology*. 2013;55(4):493-498. [CrossRef]
- Li K, Lu C, Huang Y, Yuan L, Zeng D, Wu K. Alteration of Fractional anisotropy and Mean Diffusivity in glaucoma: novel results of a meta-analysis of diffusion tensor imaging studies. *PLoS One*. 2014;9(5):e97445. Published 2014 May 14. [CrossRef]
- Trip SA, Wheeler-Kingshott C, Jones SJ, et al. Optic nerve diffusion tensor imaging in optic neuritis. *Neuroimage*. 2006;30(2):498-505. [CrossRef]
- Samson RS, Kolappan M, Thomas DL, et al. Development of a high-resolution fat and CSF-suppressed optic nerve DTI protocol at 3T: application in multiple sclerosis. *Funct Neurol*. 2013;28(2):93-100. [CrossRef]
- Nishioka C, Poh C, Sun S-W. Diffusion tensor imaging reveals visual pathway damage in patients with mild cognitive impairment and Alzheimer's disease. *J Alzheimers Dis*. 2015;45(1):97-107. [CrossRef]
- Adhikari S, Qiao Y, Singer M, et al. Retinotopic degeneration of the retina and optic tracts in autosomal dominant Alzheimer's disease. *Alzheimers Dement*. 2023;19(11):5103-5113. [CrossRef]
- Chang ST, Xu J, Trinkaus K, et al. Optic nerve diffusion tensor imaging parameters and their correlation with optic disc topography and disease severity in adult glaucoma patients and controls. *J Glaucoma*. 2014;23(8):513-520. [CrossRef]
- Newman S. Prospective study of cavernous sinus surgery for meningiomas and resultant common ophthalmic complications. *Trans Am Ophthalmol Soc*. 2007;105:392-447.
- Skeie BS, Enger PQ, Skeie GO, Thorsen F, Pedersen PH. Gamma knife surgery of meningiomas involving the cavernous sinus: long-term follow-up of 100 patients. *Neurosurgery*. 2010;4:661-668.
- Sindou M, Wydh E, Jouanneau E, Nebbal M, Lieutaud T. Long-term follow-up of meningiomas of the cavernous sinus after surgical treatment alone. *J Neurosurg*. 2007;107(5):937-944. [CrossRef]
- Vera E, Iorgulescu JB, Raper DMS, et al. A review of stereotactic radiosurgery practice in the management of skull base meningiomas. *J Neurol Surg B Skull Base*. 2014;75(3):152-158. [CrossRef]
- Klinger DR, Flores BC, Lewis JJ, Barnett SL. The treatment of cavernous sinus meningiomas: evolution of a modern approach. *Neurosurg Focus*. 2013;35(6):E8. [CrossRef]
- Fatima N, Meola A, Pollom E, Chaudhary N, Soltys S, Chang SD. Stereotactic radiosurgery in large intracranial meningiomas: a systematic review. *World Neurosurg*. 2019;129:269-275. [CrossRef]

Deep Learning–Based Diagnosis of Chondromalacia Patella from Magnetic Resonance Images

Okan Demirtaş¹, Sümeyra Kuş¹, Semih Demirel², Habib Eser Akkaya³, Oktay Yıldız¹,
Ömer Kazıcı⁴

¹Department of Computer Engineering, Gazi University Faculty of Engineering, Ankara, Türkiye

²Department of Information Systems, Gazi University Faculty of Engineering, Ankara, Türkiye

³Department of Radiology, Ankara Training and Research Hospital, Ankara, Türkiye

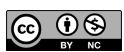
⁴Department of Radiology, Presidential Health Center, Ankara, Türkiye

Cite this article as: Demirtaş O, Kuş S, Demirel S, Eser Akkaya H, Yıldız O, Kazıcı Ö. Deep learning–based diagnosis of chondromalacia patella from magnetic resonance images. *Current Research in MRI*, 2025;4(1):12-21.

Corresponding author: Ömer Kazıcı, e-mail: omerkazci1990@gmail.com

Received: April 23, 2025 **Accepted:** May 13, 2025 **Publication Date:** August 22, 2025

DOI:10.5152/CurrResMRI.2025.25118



Content of this journal is licensed under a Creative Commons
Attribution-NonCommercial 4.0 International License.

Abstract

Objective: Chondromalacia patella is a degenerative disease of the articular cartilage in the patellofemoral joint, often leading to anterior knee pain and functional impairment. Accurate diagnosis is crucial to prevent disease progression and enable early intervention. Magnetic resonance imaging (MRI) is considered the gold standard for assessing cartilage integrity; however, manual interpretation is subjective and requires expert radiologists. In this study, a deep learning–based approach is proposed for the automatic classification of chondromalacia patella from MRI scans. A novel and domain-specific dataset was constructed for this study, consisting of labeled knee MRI scans obtained from routine clinical examinations.

Methods: This dataset is one of the first dedicated to chondromalacia patella classification, enhancing its originality and contribution to the field. The dataset was carefully curated and labeled by expert radiologists to ensure high diagnostic accuracy. It includes a diverse range of MRI images representing different grades of chondromalacia patella, making it a valuable resource for deep learning applications in musculoskeletal imaging.

Results: Three different models were evaluated: a custom-designed convolutional neural network (CNN) model and 2 pretrained architectures, VGG16 and ResNet50. Each model was trained and tested independently. The results indicate that both the custom CNN model and the VGG16 model achieved an accuracy of 92.66%, while the ResNet50 model performed slightly lower with an accuracy of 90.83%. Despite recent advancements in deep learning for musculoskeletal imaging, studies focusing specifically on chondromalacia patella remain limited.

Conclusion: This study addresses this gap by presenting an automated and objective diagnostic method that significantly enhances diagnostic accuracy. The results demonstrate the potential of deep learning methods in providing objective and highly accurate diagnoses from MRI scans, reducing the subjectivity associated with manual evaluation and offering a reliable decision-support tool for clinicians.

Keywords: Chondromalacia patella, convolutional neural networks, deep learning, MRI classification, transfer learning

INTRODUCTION

Chondromalacia patella is a degenerative condition affecting the articular cartilage of the patellofemoral joint, one of the most critical structures of the knee. This condition frequently manifests as anterior knee pain and functional impairment, particularly in young and physically active individuals, often occurring during or after sports activities.¹ According to the PearlDriver database, between 2007 and 2011, a total of 30 108 510 patients were recorded in the United States, among whom 2 188 753 individuals were diagnosed with patellofemoral pain (PFP). Of these cases, 437 711 were identified as chondromalacia patella, accounting for 20% of all PFP patients. Furthermore, the incidence of chondromalacia patella was 60% in females and 40% in males.² Chondromalacia patella, one of the potential causes of Patellofemoral Pain Syndrome, constitutes approximately 10%-25% of all visits to physical therapy clinics.³ The structural integrity and friction-reducing properties of cartilage are essential for joint health; however, its limited self-repair capacity underscores the progressive nature of chondromalacia patella. Therefore, accurate and early diagnosis is crucial for preventing the deterioration of cartilage and determining appropriate treatment strategies.⁴

Traditional diagnostic methods include clinical examination, physical tests, and imaging techniques. Among these, magnetic resonance imaging (MRI) is considered the gold standard for evaluating chondromalacia patella due to its high-contrast and detailed visualization of cartilage structures.⁵ Magnetic resonance imaging can reveal both morphological and subtle compositional changes in the cartilage. Despite these advantages, the interpretation of MRI results is a subjective process that requires substantial expertise. Radiologists' assessments can vary, and subtle early-stage cartilage lesions might be overlooked, leading to diagnostic delays.⁶ These limitations highlight the need for more objective and reproducible diagnostic methods to support clinical decision-making.

A novel and domain-specific dataset was constructed for this study, consisting of labeled knee MRI scans obtained from routine clinical examinations. Given that there is no publicly available dataset specifically for chondromalacia patella, this study provides an important contribution by introducing an original dataset that can support future research. The dataset was carefully curated and labeled by expert radiologists to ensure high diagnostic accuracy. It includes a diverse range of MRI images representing different grades of chondromalacia patella, making it a valuable resource for deep learning applications in musculoskeletal imaging.

Recent advancements in artificial intelligence and deep learning have facilitated significant progress in the development of automated diagnostic systems for medical imaging. Deep learning models, particularly convolutional neural networks (CNNs), are capable of detecting micro-level tissue abnormalities and pathological changes that may not be easily discernible by the human eye by leveraging large-scale datasets for training.⁷ In the assessment of patellar cartilage, these algorithms have demonstrated high accuracy in detecting early-stage lesions and reliably classifying disease severity.⁸ Consequently, deep learning-based approaches hold substantial potential for expediting diagnostic processes and enhancing objective clinical evaluations.

Deep learning models have increasingly been integrated with MRI data for the diagnosis of various musculoskeletal conditions. Training these models on large patient cohorts has demonstrated their ability to accurately detect different pathological stages of cartilage degeneration. Additionally, their high sensitivity and specificity in identifying microscopic early-stage tissue alterations provide a significant advantage in guiding timely therapeutic interventions.^{9,10} As a result, the development of automated and objective diagnostic systems offers promising advancements for both clinical practice and medical research by improving disease monitoring and treatment planning.

However, despite these technological advancements, the application of deep learning specifically to chondromalacia patella diagnosis remains underexplored. Most existing research on knee MRI has focused on broader pathologies or related cartilage conditions—such as fully automated detection of general cartilage lesions in the knee¹¹ or the classification of knee osteoarthritis severity from MRI.¹² Comparatively little attention has been given to developing automated methods for diagnosing patellofemoral cartilage lesions like chondromalacia patella. This gap in the literature highlights the need for a targeted investigation into whether deep learning can be effectively applied to detect chondromalacia patella from routine MRI data. Addressing this need, the present study proposes a deep learning-based approach for the automatic classification of chondromalacia patella using knee MRI scans. A custom CNN architecture was developed and trained from scratch on annotated

MRI images, and in addition, 2 state-of-the-art pretrained CNN models (VGG16 and ResNet50) were fine-tuned on the same dataset for transfer learning. Each model was trained and validated independently on a large set of labeled patellofemoral cartilage images (classified as CMP for chondromalacia and normal for healthy cartilage), and their diagnostic performance in distinguishing chondromalacia patella was systematically evaluated. By implementing and comparing both a novel, domain-specific CNN and established deep learning architectures, this study provides a comprehensive assessment of deep learning's applicability to chondromalacia patella detection.

The experimental findings demonstrate the efficacy of the proposed approach. Both the custom-designed CNN and the transfer learning-based VGG16 model achieved high classification accuracy (~92.7% on the test set), while the ResNet50 model attained a slightly lower accuracy (~90.8%). This level of performance is notable, as it approaches the reliability of expert human interpretation and significantly exceeds chance, indicating that subtle cartilage abnormalities associated with chondromalacia patella can be recognized consistently by deep learning models.

These results confirm the considerable potential of deep learning in providing objective and highly accurate diagnoses from MRI scans, directly addressing the subjectivity and variability inherent in manual MRI evaluation. The ability of the models to detect chondromalacia patella with such high accuracy underscores how artificial intelligence can augment clinical practice—particularly as a decision-support tool that identifies early-stage cartilage lesions for further review, thereby facilitating earlier interventions.

In the context of the literature, this work represents a significant advancement in automated medical diagnostics for musculoskeletal imaging. To the authors' knowledge, it is one of the first studies to focus explicitly on chondromalacia patella classification using deep learning, thereby filling an important gap in the domain of knee cartilage assessment.

Overall, the study not only introduces an effective AI-driven solution for a specific diagnostic challenge but also advances the current state of knowledge by demonstrating that deep learning can be successfully harnessed for patellofemoral cartilage evaluation. This contribution lays the groundwork for future research and development of AI-assisted diagnostic tools in orthopedics, ultimately aiming to improve diagnostic accuracy and patient outcomes for knee joint disorders.

MATERIAL AND METHODS

The knee MRI data used in this study were obtained from routine clinical examinations at Ankara Training and Research Hospital. All procedures were approved by the institutional Ethics Committee of Gazi University (Approval No: 1117365; Date: 13.12.2024). As this was a retrospective study, the imaging data were obtained from an existing database; therefore, informed consent was not required. Imaging was performed using a 1.5 Tesla MRI scanner (Siemens) with T2-weighted and Proton Density sequences at a slice thickness of 3 mm and in-plane matrix size of 512 × 512 (field of view 16 cm). Images in sagittal, coronal, and axial planes focusing on the patellofemoral joint were included to capture the cartilage from multiple views. The dataset was categorized into 2 classes: chondromalacia patella (CMP) and normal (Figure 1). In total, 1073 MRI slice images were collected, with 648 labeled as CMP and 425 as normal. For model development and evaluation, the data were stratified and split into training, validation, and

MAIN POINTS

- Understand the role of deep learning in diagnosing chondromalacia patella from magnetic resonance imaging (MRI) scans.
- Recognize the importance of creating a dedicated and expertly labeled MRI dataset for accurate model training.
- Compare the diagnostic performance of different convolutional neural network architectures, including custom and pretrained models.
- Evaluate the potential of artificial intelligence-based systems to support clinical decision-making and reduce diagnostic subjectivity.

test subsets, as illustrated in Figure 2. The training set consisted of 858 images (518 CMP, 340 normal), the validation set contained 106 images (64 CMP, 42 normal), and the test set included 109 images (66 CMP, 43 normal). This stratified split ensured a balanced representation of both classes across all subsets, facilitating robust model training and evaluation. All images were initially assessed by a specialist musculoskeletal radiologist, and a second independent radiologist reviewed the labels to ensure diagnostic accuracy. Low-quality or artefactual scans were excluded prior to analysis. Before input to the deep learning models, all MR images underwent standard preprocessing. Each image was resized to 224×224 pixels to fit the input requirements of the CNN models. Intensity values were normalized to the range $[0, 1]$ by linear scaling of pixel values, which facilitates network training and convergence. To prepare for training, the training images were randomly shuffled (to eliminate any unintended ordering biases) and then batched. A mini-batch size of 32 was used, balancing convergence stability with computational efficiency. This batching, along with an optimized data pipeline (including data shuffling and prefetching), helped improve training throughput and prevented the model from learning spurious sequential patterns. No additional data augmentation was applied, so as to evaluate the models on the original image distributions.

Experimental Study

We developed a custom CNN architecture for the binary classification of chondromalacia patella. The network consisted of 4 convolutional blocks followed by fully connected layers (Figure 3). In the first convolutional layer, 32 filters of size 3×3 were applied to extract low-level visual features from the input MR images. A Rectified Linear Unit (ReLU) activation was used after each convolution to introduce nonlinearity, defined as (1):

$$f(x) = \max(0, x) \quad (1)$$

Each convolutional block also included a 2×2 max-pooling layer that down-sampled feature maps (reducing spatial dimensions by a factor of 2) to highlight the most salient features and reduce computational complexity. As the network depth increased, the number of filters in convolutional layers was doubled ($32 \rightarrow 64 \rightarrow 128 \rightarrow 256$) in successive blocks to learn more complex and abstract feature representations.

To mitigate overfitting, dropout regularization¹³ was incorporated after certain layers. For example, after the first convolutional block, a dropout layer with a rate of 0.2 was applied—meaning each neuron in that

layer was retained with a probability of 0.8 and dropped with a probability of 0.2 during training. Similar dropout layers with increasing drop rates (0.3, 0.4, and 0.5 in subsequent blocks) were used as the network grew deeper, progressively randomizing neuron activations to encourage generalization. The output feature maps from the final convolutional layer were flattened into a one-dimensional vector, which was then fed into a dense fully connected layer of 256 neurons. This dense layer also used ReLU activation to learn high-level combinations of the extracted features. Another dropout layer (50% rate) followed the dense layer to further reduce overfitting.

Finally, the network's output layer was a single neuron with a sigmoid activation function, producing a probability between 0 and 1 to indicate the likelihood of the input image being classified as chondromalacia. The sigmoid function is defined as (2):

$$\sigma(x) = \frac{1}{1 + e^{-x}} \quad (2)$$

where x represents the input to the activation function. The sigmoid function squashes the input into a range between 0 and 1, making it particularly suitable for binary classification problems such as chondromalacia detection. The function ensures that outputs can be interpreted as probabilities, which facilitates decision-making in the classification process.

In summary, the custom CNN architecture was designed to progressively extract features through convolution and pooling while using ReLU activations and dropout regularization to ensure robust learning and prevent overfitting.

In the second phase of the study, transfer learning was employed to evaluate the performance of pretrained VGG16¹⁴ and ResNet50¹⁵ models. Transfer learning is based on the principle of utilizing pretrained models with frozen lower-layer weights while retraining only the upper layers for a specific target dataset, as illustrated in Figures 4 and 5.

Depending on the model selection, VGG16 or ResNet50 was loaded with pretrained weights from the ImageNet dataset, while the fully connected layers were excluded (include_top=False). This approach preserved the feature extraction capabilities of the original model, ensuring that only the classification layer was retrained for the target dataset.

Initially, all layers of the base models were frozen (trainable=False). However, to enhance generalization, in the VGG16 model, the first 10

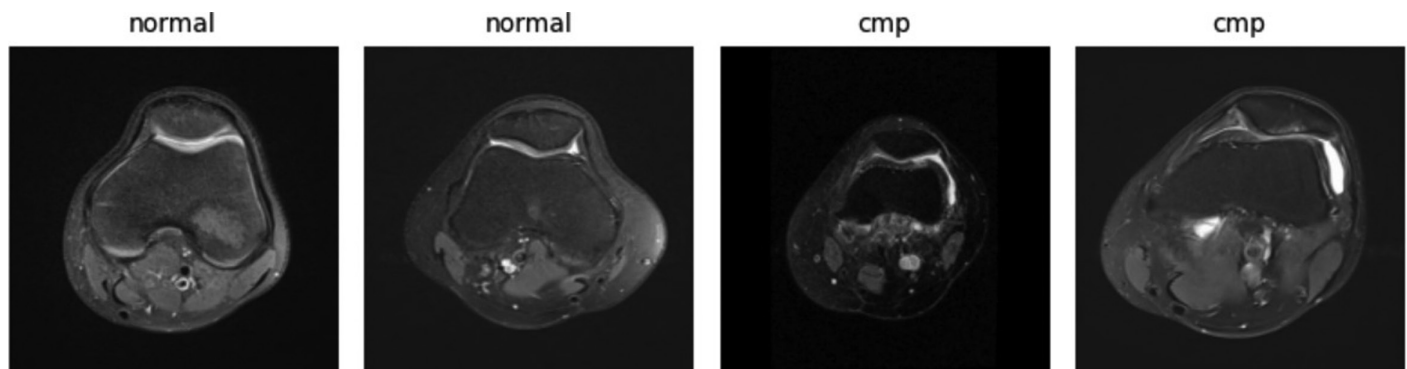


Figure 1. Examples of the dataset.

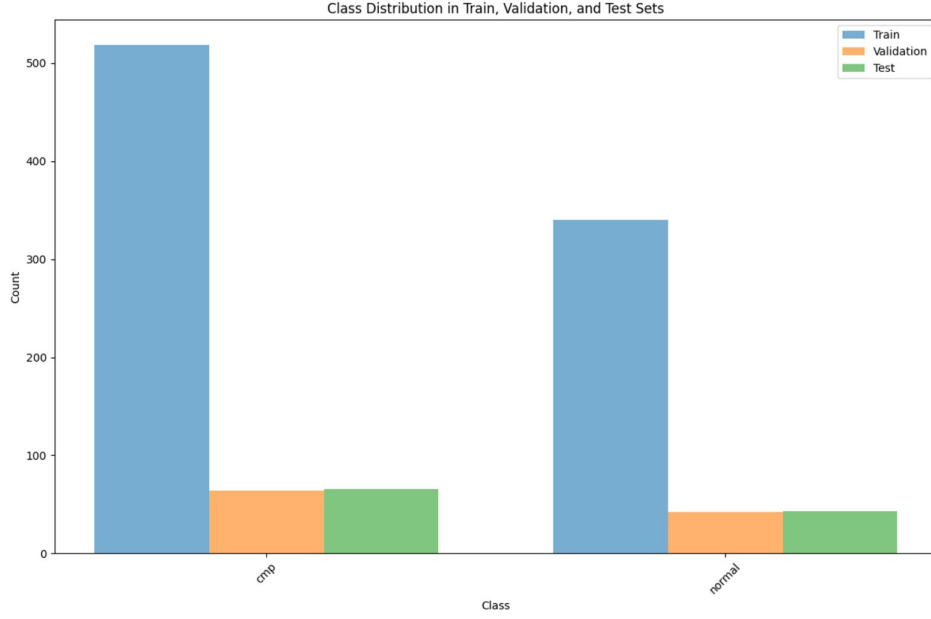


Figure 2. Distribution of the dataset across training, validation, and test sets for chondromalacia patella and normal classes.

layers were frozen while the remaining layers were made trainable, whereas in the ResNet50 model, the last 20 layers were fine-tuned to adapt the model to the target dataset.

The feature maps extracted from the base model were processed through a Global Average Pooling (GAP) layer. The GAP layer computes the mean activation of each feature map, reducing the number of trainable parameters and mitigating the risk of overfitting.

Following the GAP layer, a fully connected (dense) layer with 128 neurons and a ReLU activation function was incorporated. To further prevent overfitting, a 50% dropout layer was applied. Finally, a single neuron with a sigmoid activation function was used in the output layer for binary classification.

All models (the custom CNN and the 2 transfer learning models) were trained using a consistent procedure to ensure a fair comparison. The network weights were optimized using the Adam optimization algorithm, which is an adaptive stochastic gradient descent method. Adam maintains moving averages of the gradient and its square to adapt the learning rate for each parameter. At each training step t , the first moment m_t (mean of gradients) and second moment v_t (uncentered variance) are updated as (3-4):

$$m_t = \beta_1 m_{t-1} + (1 - \beta_1) g_t \quad (3)$$

$$v_t = \beta_2 v_{t-1} + (1 - \beta_2) g_t^2 \quad (4)$$

where g_t is the gradient of the loss with respect to the model parameters at step t , and β_1 and β_2 are the decay rates for the moving averages (typically $\beta_1 = 0.9$, $\beta_2 = 0.999$). The learning rate was initially set to 1×10^{-4} for all experiments, as this small rate provided stable learning for

complex models. Model parameters were updated using backpropagation to minimize the classification loss.

The binary cross-entropy loss function is employed, which is suitable for binary classification problems. This loss function measures the discrepancy between predicted probabilities and true labels, and is defined as (5):

$$L = -\frac{1}{N} \sum_{i=1}^N [y_i \log(y_i) + (1 - y_i) \log(1 - y_i)] \quad (5)$$

where:

- N is the total number of training samples,
- $y_i \in \{0, 1\}$ is the true label of sample i (with 1 representing chondromalacia patella and 0 representing normal cartilage),
- \hat{y}_i is the predicted probability that sample i belongs to the positive class (CMP).

This loss function penalizes confident misclassifications heavily, guiding the optimizer towards improved predictions.

During training, dropout layers were activated as described in the model architecture. This means that in each iteration, different subsets of neurons were randomly dropped, helping the Adam optimizer generalize the model. Training was carried out in mini-batches of 32 images, striking a balance between computational efficiency and gradient estimation stability. The models were trained for a maximum of 100 epochs or until convergence.

To prevent overfitting, an early stopping strategy was implemented based on validation performance. Specifically, if the validation loss did not improve for a patience period of 10 consecutive epochs, training was halted. The model parameters corresponding to the epoch with the lowest validation loss were then restored as the final model.

Model: "sequential"

Layer (type)	Output Shape	Param #
conv2d (Conv2D)	(None, 222, 222, 32)	896
max_pooling2d (MaxPooling2D)	(None, 111, 111, 32)	0
dropout (Dropout)	(None, 111, 111, 32)	0
conv2d_1 (Conv2D)	(None, 109, 109, 64)	18496
max_pooling2d_1 (MaxPooling2D)	(None, 54, 54, 64)	0
dropout_1 (Dropout)	(None, 54, 54, 64)	0
conv2d_2 (Conv2D)	(None, 52, 52, 128)	73856
max_pooling2d_2 (MaxPooling2D)	(None, 26, 26, 128)	0
dropout_2 (Dropout)	(None, 26, 26, 128)	0
conv2d_3 (Conv2D)	(None, 24, 24, 256)	295168
max_pooling2d_3 (MaxPooling2D)	(None, 12, 12, 256)	0
dropout_3 (Dropout)	(None, 12, 12, 256)	0
flatten (Flatten)	(None, 36864)	0
dense (Dense)	(None, 256)	9437440
dropout_4 (Dropout)	(None, 256)	0
dense_1 (Dense)	(None, 1)	257
=====		
Total params: 9826113 (37.48 MB)		
Trainable params: 9826113 (37.48 MB)		
Non-trainable params: 0 (0.00 Byte)		

Figure 3. The structure of the custom neural network.

This ensured that the best-performing model on validation data was retained rather than one that might have started overfitting with continued training.

The entire training process was executed using the TensorFlow/Keras deep learning framework. Model training and validation were performed on an NVIDIA GPU, which accelerated the computation of convolution operations and gradient updates. By the end of training, 3 trained models were obtained (the custom CNN, VGG16-based, and ResNet50-based), each with learned parameters optimized to distinguish chondromalacia patella from normal cartilage in MRI slices.

Results

After training, each model's performance was evaluated on the held-out test set using standard classification metrics. The focus was on metrics that reflect both overall accuracy and the model's ability to correctly identify the positive class (chondromalacia patella).

Accuracy was calculated as the proportion of correctly classified images among all test images (6):

$$\text{Accuracy} = \frac{\text{TP} + \text{TN}}{\text{TP} + \text{TN} + \text{FP} + \text{FN}} \quad (6)$$

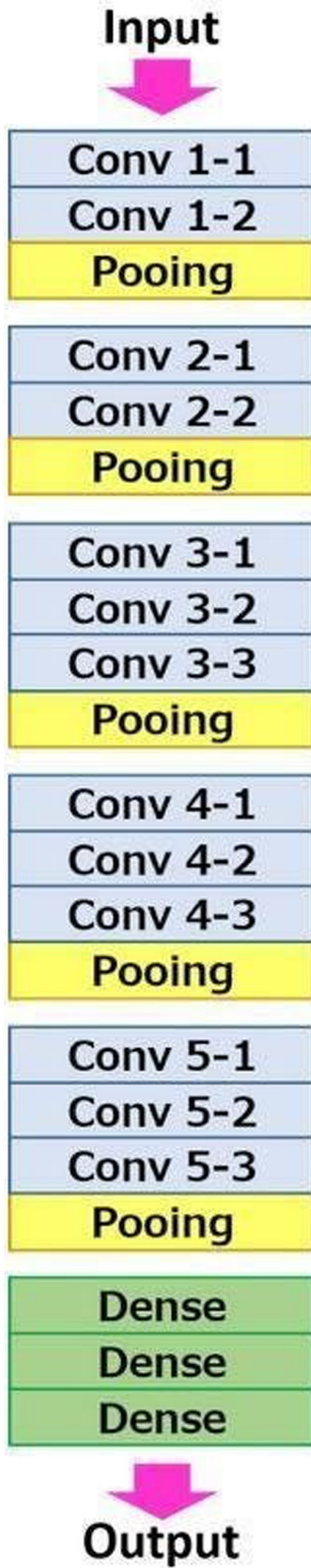


Figure 4. VGG16 model architecture.

where:

- TP (True Positives) - Correctly predicted chondromalacia cases.
- TN (True Negatives) - Correctly predicted normal cases.
- FP (False Positives) - Normal cases incorrectly predicted as chondromalacia.
- FN (False Negatives) - Chondromalacia cases incorrectly predicted as normal.

While accuracy provides an overall measure of performance, it can be less informative when dealing with imbalanced datasets. Therefore, additional evaluation metrics were used to assess the model's performance more comprehensively.

Precision, also known as positive predictive value, measures how reliable the model's chondromalacia predictions are. It is defined as (7):

$$\text{Precision} = \frac{\text{TP}}{\text{TP} + \text{FP}} \quad (7)$$

A higher precision indicates that when the model predicts chondromalacia, it is often correct. High precision minimizes false alarms, which is particularly important in clinical applications where unnecessary interventions should be avoided.

Recall, also known as sensitivity, measures how well the model identifies true chondromalacia cases. It is given by (8):

$$\text{Recall} = \frac{\text{TP}}{\text{TP} + \text{FN}} \quad (8)$$

A high recall means that the model is effective at detecting chondromalacia and misses few actual cases, which is crucial for ensuring that patients with the condition are correctly identified.

To balance precision and recall, the F1-score is computed, which is the harmonic mean of precision and recall (9):

$$F1 = \frac{2 \times \text{Precision} \times \text{Recall}}{\text{Precision} + \text{Recall}} \quad (9)$$

The F1-score is particularly useful when the positive class (chondromalacia) is of primary importance. It provides a single metric that reflects both the reliability of positive predictions and the ability to detect true cases.

To further analyze the model's classification performance, the confusion matrix is computed, which compares the model's predictions with the ground-truth labels on the test set. This structured representation details the number of correctly and incorrectly classified samples across different categories.

In reporting results, the emphasis was on both accuracy and F1-score as indicators of overall effectiveness, while precision and recall provide further insight into the model's ability to correctly identify chondromalacia cases. These metrics help assess the model's capability to detect chondromalacia while minimizing false positives and false negatives, ensuring both high sensitivity and specificity in clinical applications.

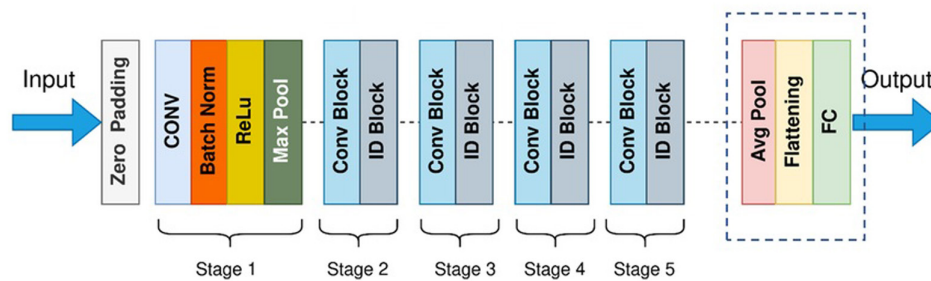


Figure 5. ResNet50 model architecture.

Table 1 the accuracy, precision, recall, and F1-score metrics obtained for each model across the training, validation, and test phases. The ResNet50 model was pretrained on the ImageNet dataset and fine-tuned by making the last 20 layers trainable. The model achieved a test accuracy of 90.83%, with precision, recall, and F1-score values of 86.67%, 90.70%, and 88.64%, respectively. The validation accuracy of ResNet50 was 90.57%, indicating that overfitting was effectively minimized and the model maintained a strong generalization capability.

Similarly, the VGG16 model was fine-tuned by unfreezing its last 10 layers, followed by training on the target dataset. The model achieved a test accuracy of 92.66 %, with precision, recall, and F1-score values of 90.70% across all metrics. The validation accuracy was 89.62%, demonstrating superior test accuracy compared to ResNet50.

The custom CNN model, designed from scratch, consisted of three convolutional blocks followed by fully connected layers. The model was trained for 42 epochs, achieving a test accuracy of 92.66%, with precision, recall, and F1-score values of 88.89%, 93.02%, and 90.91%, respectively. Notably, the validation accuracy of 96.23% suggests that the custom CNN exhibited a higher generalization performance compared to the transfer learning-based models.

Overall, the experimental results indicate that both VGG16 and the custom CNN model demonstrated superior classification performance, while ResNet50 exhibited slightly lower accuracy. The findings highlight the effectiveness of transfer learning for medical image classification, while also emphasizing the potential of custom-built architectures tailored to specific tasks.

Figure 6 presents the training and validation performance of three models: (a) Custom CNN, (b) VGG16, and (c) ResNet50. Each sub-figure displays accuracy (left) and loss (right) over training epochs. The custom CNN model shows a consistent increase in training and validation accuracy, with minor fluctuations in validation accuracy. The validation loss decreases smoothly, indicating good generalization with minimal overfitting. In contrast, the VGG16 model exhibits noticeable fluctuations in validation accuracy, suggesting instability in learning. The ResNet50 model demonstrates stable performance, with training and validation accuracy curves closely aligned. The validation loss decreases steadily and follows the training loss trend, suggesting strong generalization and minimal overfitting.

Table 2 presents the confusion matrices for Custom CNN, VGG16, and ResNet50. ResNet50 achieves the highest number of correctly classified CMP samples (62), followed by Custom CNN (61) and VGG16 (60). In the normal class, Custom CNN correctly classifies 40 instances, while

ResNet50 and VGG16 classify 39. Misclassification rates are slightly higher in VGG16, with 6 CMP samples incorrectly labeled as normal and 4 normal samples predicted as CMP. ResNet50 exhibits the lowest overall misclassification, indicating superior generalization performance.

DISCUSSION

This study demonstrates the effectiveness of deep learning models in classifying chondromalacia patella from MRI images. The comparative analysis of ResNet50, VGG16, and a custom CNN model highlights the significance of architectural selection in medical image classification. The superior performance of the custom CNN model, which achieved 92.66% test accuracy and an F1-score of 90.91%, suggests that task-specific architectures can exhibit better generalization capabilities for specific medical imaging tasks.

Deep learning-based studies on MRI analysis of musculoskeletal disorders have been previously investigated. Prior research has demonstrated the suitability of CNNs for classifying knee pathologies.¹⁶ A recent study using 3D CNNs for knee osteoarthritis classification achieved 86.5% accuracy, demonstrating the effectiveness of deep learning in musculoskeletal imaging.¹⁷ Similarly, a VGG16-based classification approach reported 86.7% accuracy, supporting the feasibility of transfer learning for knee pathology diagnosis.¹⁸

In comparison, this study showed that ResNet50 achieved 90.83% accuracy, surpassing previous models based on 3D CNNs and VGG16. However, the custom CNN model outperformed all other approaches, highlighting the importance of architecture optimization in improving classification performance. The ability of the custom CNN to achieve superior generalization suggests that designing models tailored to specific medical imaging tasks may be more effective than relying solely on transfer learning.

Furthermore, the low false positive and false negative rates observed in the confusion matrix suggest that the custom CNN model effectively distinguishes between CMP and normal cases, reducing the risk of misclassification. This improvement can be attributed to the use of dropout regularization, fine-tuned convolutional layers, and an optimized training strategy.

Additionally, the choice of the Adam optimization algorithm with a learning rate of $1e-4$ contributed to stable training performance. Studies by Kingma and Ba¹² (2014) demonstrate that Adam outperforms traditional stochastic gradient descent in medical image analysis.

The batch size of 32 was chosen based on recent findings that smaller batch sizes can improve model generalization and latent feature

Table 1. Comparison of Training, Validation, and Test Metrics

Model	Training Accuracy	Training Precision	Training Recall	Training F1 Score	Validation Accuracy	Validation Precision	Validation Recall	Validation F1 Score	Test Accuracy	Test Precision	Test Recall	Test F1 Score
ResNet50	0.9720	0.9566	0.9735	0.9650	0.9057	0.8810	0.8810	0.8810	0.9083	0.8667	0.9070	0.8864
VGG16	0.9277	0.9041	0.9147	0.9094	0.8962	0.8605	0.8810	0.8706	0.9266	0.9070	0.9070	0.9070
Custom CNN	0.9720	0.9731	0.9559	0.9644	0.9623	0.9750	0.9286	0.9512	0.9266	0.8889	0.9302	0.9091

CNN, convolutional neural network.

Table 2. Confusion Matrices for Different Models

Model	True: CMP		True: NORMAL	
	CMP	NORMAL	CMP	NORMAL
Custom CNN	61	5	3	40
VGG16	60	6	4	39
ResNet50	62	4	4	39

CMP, chondromalacia patella.

extraction in medical imaging tasks,¹⁹ while also balancing computational efficiency as demonstrated in studies with MobileNet V2 and ShuffleNet.²⁰

The superior performance of the custom CNN model can be attributed to several key factors. First, its architecture was specifically designed for chondromalacia patella detection. While standard architectures such as ResNet50 and VGG16 are pretrained on large-scale datasets like ImageNet, the custom model was optimized to focus on the distinct characteristics of musculoskeletal MRI scans. Second, the low false positive and false negative rates observed in the confusion matrix suggest that the model effectively differentiates between varying severity levels of chondromalacia patella.

From a clinical perspective, the implementation of deep learning models for MRI-based chondromalacia patella diagnosis offers several advantages. One of the most notable benefits is the reduction of inter-observer variability, which is a common challenge in radiological assessments. Studies have reported inconsistencies in manual grading and interpretation of MRI scans, highlighting the need for automated decision-support systems to enhance diagnostic reliability and standardization.⁶

The high classification accuracy and F1-score achieved by the custom CNN model suggest that deep learning can provide objective and reproducible evaluations, assisting radiologists and medical specialists in clinical decision-making.^{7,8} Furthermore, deep learning-based classification can significantly reduce interpretation time, allowing for more efficient and timely diagnoses, ultimately improving patient management and treatment planning.

This study highlights the effectiveness of deep learning models, particularly a custom-designed CNN, in diagnosing chondromalacia patella from MRI scans. The experimental results demonstrate that the custom CNN and VGG16 models achieve superior performance, while ResNet50 exhibits slightly lower accuracy. The findings emphasize the potential of custom-built architectures and transfer learning in medical image classification, while also underscoring the importance of further research into domain-specific optimizations. Despite the promising results, this study has several limitations. A primary concern is the limited dataset size, which may affect the model's generalizability across diverse patient populations. Utilizing larger and more varied MRI datasets could enhance model robustness and clinical applicability. Studies have shown that deep learning models trained on extensive and heterogeneous data perform better across different clinical settings. Another significant issue is the domain gap between natural images used in pretrained models (e.g., ImageNet) and medical images like MRI scans. This disparity can limit the effectiveness of transfer learning in medical imaging applications. Research indicates that models pretrained on medical-specific datasets, such as RadImageNet, outperform those trained on natural image datasets, underscoring the importance of domain-specific pretraining. Future

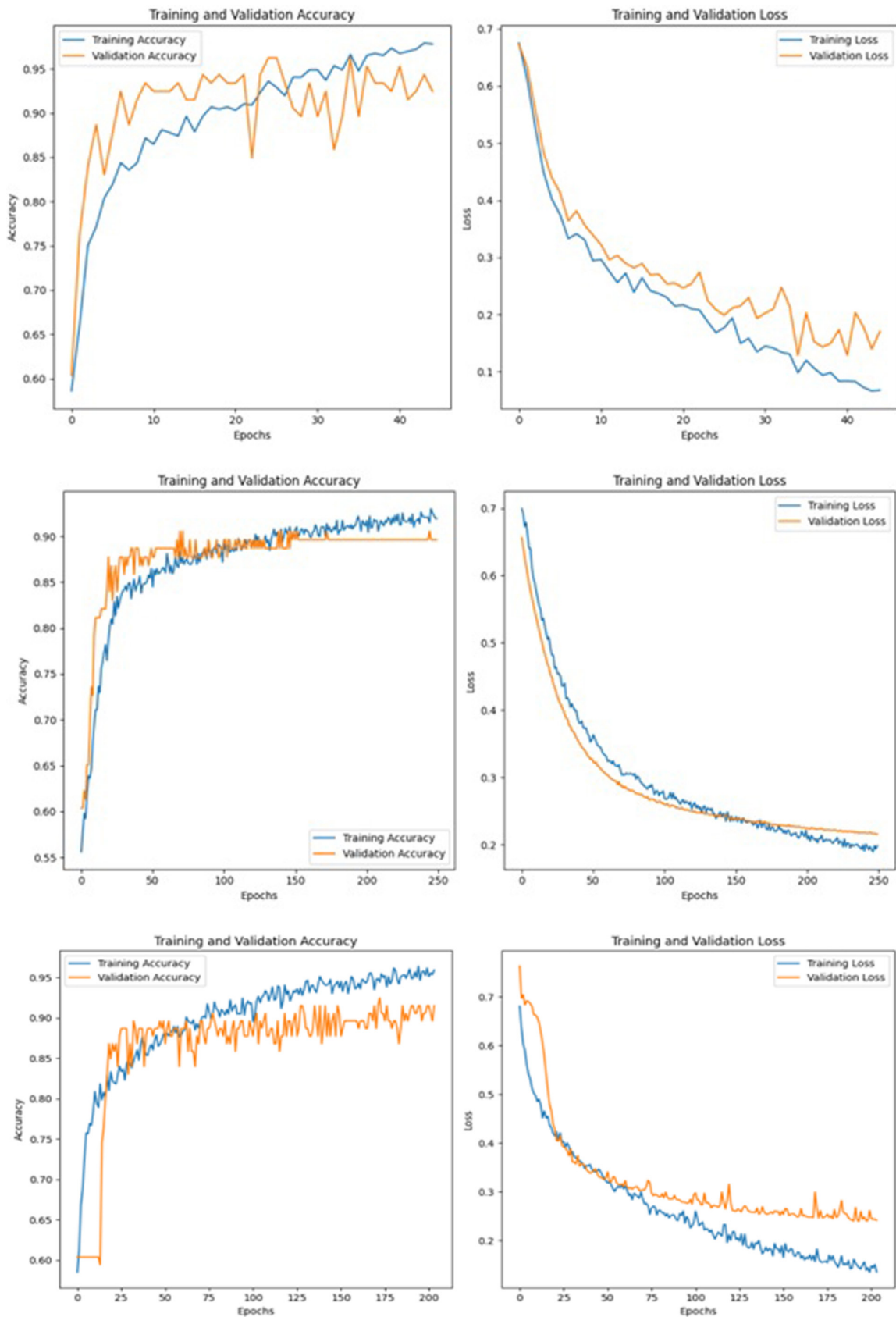


Figure 6. Comparison of training and validation performance across different models. (A) Training and validation accuracy/loss of custom CNN. (B) Training and validation accuracy/loss of VGG16. (C) Training and validation accuracy/loss of ResNet50.

work should focus on improving scalability, expanding the dataset, and developing fully automated deep learning pipelines to enhance clinical applicability. Given the scarcity of labeled medical imaging data, exploring semi-supervised learning techniques presents a viable alternative. Methods like self-supervised learning have shown promise in leveraging unlabeled data to improve model performance in medical image analysis. Additionally, incorporating training models on medical-specific datasets may further improve generalization. By addressing these aspects, deep learning approaches can contribute more effectively to the automated diagnosis of musculoskeletal conditions, ultimately improving clinical decision-making and patient outcomes.

Data Availability Statement: The data that support the findings of this study are available on request from the corresponding author.

Ethics Committee Approval: This study was approved by the institutional ethics committee of Gazi University (Approval No: 1117365; Date: 13.12.2024).

Informed Consent: As this was a retrospective study, the imaging data were obtained from an existing database; therefore, informed consent was not required.

Peer-review: Externally peer-reviewed.

Author Contributions: Concept – O.O.; Design – O.S.; Supervision – O.O.; Resources – S.S.; Materials – O.H.; Data Collection and/or Processing – O.H.; Analysis and/or Interpretation – S.S.; Literature Search – O.O.; Writing Manuscript – O.O.; Critical Review – O.O.; Other – S.S.





Declaration of Interests: The authors have no conflict of interest to declare.

Funding: The authors declared that this study has received no financial support.

REFERENCES

- McConnell J. The physical therapist's approach to patellofemoral disorders. *Clin Sports Med*. 2002;21(3):363-387. [\[CrossRef\]](#)
- Glaviano NR, Kew M, Hart JM, Saliba S. Demographic and epidemiological trends in patellofemoral pain. *Int J Sports Phys Ther*. 2015;10(3):281-290.
- Pak J, Lee JH, Lee SH. A novel biological approach to treat chondromalacia patellae. *PLoS One*. 2013;8(5):e64569. [\[CrossRef\]](#)
- Powers CM. The influence of altered lower-extremity kinematics on patellofemoral joint dysfunction: a theoretical perspective. *J Orthop Sports Phys Ther*. 2003;33(11):639-646. [\[CrossRef\]](#)
- Cucchiari M, De Girolamo L, Filardo G, et al. Basic science of osteoarthritis. *J Exp Orthop*. 2016;3(1):22. [\[CrossRef\]](#)
- Recht M, Bobic V, Burstein D, et al. Magnetic resonance imaging of articular cartilage. *Clinical orthopaedics and related Research*. 2001;391:379-396.
- Litjens G, Kooi T, Bejnordi BE, et al. A survey on deep learning in medical image analysis. *Med Image Anal*. 2017;42:60-88. [\[CrossRef\]](#)
- Shen D, Wu G, Suk H-I. Deep learning in medical image analysis. *Annu Rev Biomed Eng*. 2017;19(1):221-248. [\[CrossRef\]](#)
- Gold GE, Han E, Stainsby J, Wright G, Brittain J, Beaulieu C. Musculoskeletal mri at 3.0 t: relaxation times and image contrast. *AJR Am J Roentgenol*. 2004;183(2):343-351. [\[CrossRef\]](#)
- Schipphof D. *Identifying Knee Osteoarthritis*. Dutch Arthritis Foundation. Amsterdam. Rotterdam: Optima Grafische Communicatie; 2011.
- Liu F, Zhou Z, Samsonov A, et al. Deep learning approach for evaluating knee mr images: achieving high diagnostic performance for cartilage lesion detection. *Radiology*. 2018;289(1):160-169. [\[CrossRef\]](#)
- Kingma DP, Ba J. Adam: a method for stochastic optimization. *arXiv Preprint ArXiv:1412.6980* 2014.
- Hinton GE, Srivastava N, Krizhevsky A, Sutskever I, Salakhutdinov RR. Improving neural networks by preventing co-adaptation of feature detectors. *arXiv Preprint ArXiv:1207.0580* 2012.
- Simonyan K, Zisserman A. Very deep convolutional networks for large-scale image recognition. *arXiv Preprint ArXiv:1409.1556* 2014.
- He K, Zhang X, Ren S, Sun J. Deep residual learning for image recognition. In: *Proceedings of the IEEE Conference on Computer Vision and Pattern Recognition*. New York: IEEE; 2016:770-778. [\[CrossRef\]](#)
- Bien N, Rajpurkar P, Ball RL, et al. Deep-learning-assisted diagnosis for knee magnetic resonance imaging: development and retrospective validation of mrnet. *PLoS Med*. 2018;15(11):e1002699. [\[CrossRef\]](#)
- Guida C, Zhang M, Shan J. Knee osteoarthritis classification using 3d CNN and mri. *Appl Sci*. 2021;11(11):5196. [\[CrossRef\]](#)
- Solak FZ. Classification of knee osteoarthritis severity by transfer learning from x-ray images. *Karaelmas Fen Ve Muhendislik Dergisi*. 2024;14(2):119-133.
- Kerley CI, Cai LY, Tang Y, et al. Batch size go big or go home: counter-intuitive improvement in medical autoencoders with smaller batch size. In: *Medical Imaging: Image Processing*. 2023;12464:106-115. SPIE
- Biswas K, Pal R, Patel S, et al. A novel momentum-based deep learning techniques for medical image classification and segmentation. In: *Berlin: International Workshop on Machine Learning in Medical Imaging*; 2024:1-11. Springer

Effect of Breast Fibroglandular Tissue Density in Tumor Visualization and Characterization on Diffusion MRI

Hatice Ayça Ata Korkmaz¹, Sibel Kul¹, İlker Eyüboğlu¹, Mehmet Şükrü Oğuz¹, İsmet Miraç Çakır², Süleyman Bekirçavuşoğlu³

¹Department of Radiology, Karadeniz Technical University Faculty of Medicine, Trabzon, Türkiye

²Department of Radiology, Samsun University Faculty of Medicine, Samsun, Türkiye

³Department of Radiology, University of Health Sciences, Bursa City Hospital, Bursa, Türkiye

Cite this article as: Korkmaz HAA, Kul S, Eyüboğlu İ, et al. Effect of breast fibroglandular tissue density in tumor visualization and characterization on diffusion MRI. *Current Research in MRI*, 2025;4(1):22-26.

Corresponding author: Hatice Ayça Ata Korkmaz, e-mail: dr.h.aycaatakorkmaz@gmail.com

Received: April 17, 2025 **Accepted:** May 22, 2025 **Publication Date:** August 22, 2025

DOI: 10.5152/CurrResMRI.2025.25109



Content of this journal is licensed under a Creative Commons Attribution-NonCommercial 4.0 International License.

Abstract

Objective: This study aimed to investigate the effect of breast fibroglandular tissue density on tumor visibility and characterization efficacy in diffusion-weighted magnetic resonance imaging (DWI-MRI).

Methods: After ethics committee approval from Karadeniz Technical University (No: 2025/16, Date: 25.03.2025), 2 independent readers retrospectively evaluated the images of 216 consecutive patients (age range, 16-85 years; mean, 45.5 years) who underwent breast MRI for suspicious clinical-radiological findings and later received a definite diagnosis. Only diffusion-weighted images were used at all stages of evaluation. Evaluation parameters were tumor visibility (4-point scale), malignancy probability (7-point scale), and tumor apparent diffusion coefficient (ADC) value. The most suspicious single index lesion was evaluated for each patient. The malignancy scores were determined by considering the morphologic features and the signal of tumors on the ADC map. The ADC values were measured manually on an MRI workstation. Later on, breast densities determined jointly by the readers using T1-weighted images according to the Breast Imaging Reporting and Data System (BI-RADS) classification. Student's *t*-test, Chi-square test, and receiver operating characteristic analysis were used to statistically compare tumor visibility and diagnostic efficacies in different breast density groups (A, B=non-dense, C, D=dense).

Results: Of the 216 patients, 116 (54%) had dense while 100 (46%) had non-dense breast tissue. Around 131 (61%) of the lesions were malignant and 85 (39%) were benign. In 80%-90% of cases with either dense or non-dense breasts, high-moderate tumor visibility was obtained. There was no significant difference between the dense and non-dense breasts in terms of tumor visibility ($P \geq .216$) (Table 1). The mean ADC value in malignant tumors was lower than in benign tumors ($P < .001$). The agreement between the malignancy scores of the readers was moderate ($\kappa=0.597$, $P < .001$). Diagnostic accuracy values in dense breasts were generally higher than in non-dense breasts (Tables 2 and 3). However, for neither of the evaluation methods nor readers, the result was statistically significant ($P \geq .154$).

Conclusion: In dense breasts, the risk of cancer is higher and the diagnostic efficacy of mammography is low. Therefore, additional methods are needed to increase the diagnostic efficacy in malignant tumors. Diffusion MRI is a very popular, highly efficient, easy-to-apply non-contrast-enhanced MR-based molecular imaging method. It has become a standard in routine clinical applications as an adjunct to breast dynamic contrast-enhanced MRI but it is also suitable for standalone use.

In conclusion, malignant tumors are highly visible on diffusion MRI and differentiation of malignant from benign tumors can be made with 80%-90% accuracy regardless of breast density. It provides both qualitative and quantitative data. Qualitative data might also be used to grade malignancy probability like in the BI-RADS system. As a result, especially in dense breasts, diffusion MRI might be used in addition to mammography to improve the cancer detection ability.

Keywords: Breast, Diffusion-weighted MRI, DWI-MRI, Fibroglandular tissue density

INTRODUCTION

Breast cancer is a relatively common and potentially life-threatening serious disease that affects millions of women globally.¹ The diagnosis of breast cancer on mammography is limited in dense breast. While the detection rate is close to 100% in American College of Radiology (ACR) type 1 fibroglandular breast density, this rate decreases to 50% in ACR type 4 dense breast patterns.²

Breast density, a significant patient-specific variable, is one of the most critical determinants of diagnostic accuracy in mammography. The presence of dense fibroglandular tissue not only indicates an increased risk of cancer (4-6 fold) but also diminishes diagnostic efficacy in mammography.³ Consequently, patients with dense breast patterns require additional modalities to enhance diagnostic accuracy.⁴

Magnetic resonance imaging (MRI) is a valuable complementary imaging modality to mammography and ultrasound for the assessment of suspicious breast lesions.⁵ Despite its high diagnostic accuracy, its limited accessibility, high cost, time-consuming nature, and requirement for contrast

agents restrict its widespread use. Consequently, while its utility in improving cancer detection in dense breasts is well-established, it has not been universally adopted for screening purposes.

Research is ongoing to enhance the diagnostic specificity of breast MRI through the development of novel imaging sequences and post-processing algorithms. In this context, diffusion-weighted imaging has emerged as a valuable tool for breast lesion characterization, being increasingly incorporated into routine MRI protocols in recent years.⁶

Diffusion-weighted magnetic resonance imaging (DWI-MRI) is a non-invasive imaging modality that provides both qualitative and quantitative data without the need for contrast agents.

Diffusion-weighted imaging is a non-invasive molecular imaging modality that quantifies the random Brownian motion of water molecules within tissues. This technique characterizes tissue microstructure, with the diffusion of water molecules being primarily influenced by tissue cell density. The apparent diffusion coefficient (ADC) is a quantitative parameter used to assess the degree of diffusion.⁷

The DWI-MRI is an advanced radiological imaging technique that has demonstrated high efficacy in characterizing breast tumors.⁸ Key parameters assessed in DWI include the ADC value, DWI signal intensity, and tumor morphology. By evaluating ADC values and tumor morphology, DWI can differentiate between benign and malignant tumors with an accuracy of 80%-90%.

To assess the potential utility of DWI-MRI as an alternative diagnostic modality in patients with dense breast tissue, it is crucial to evaluate the efficacy of DWI in visualizing and characterizing breast tumors.

This study aimed to evaluate the effect of breast fibroglandular tissue density on tumor visualization and characterization in DWI-MRI.

MATERIAL AND METHODS

Subjects

This retrospective study received approval from the Karadeniz Technical University Ethics Committee (Approval no: 2025/16 Date: March 25, 2025). Written informed consent forms were obtained from all patients participating in the study.

After ethical community approval, 2 independent readers (R1 and R2) retrospectively evaluated DWI MR images of 216 consecutive patients (age range, 16-85 years; mean, 45.5 years) who underwent breast MRI due to suspicious clinical-radiological findings and received a definitive diagnosis.

Of the total cases, 189 received a definitive diagnosis based on histopathological examination of surgically excised or needle-biopsied

Table 1. Tumor Visibility at Different Breast Densities

Breast Density	Average Visibility Score	
	R1	R2
Non-dense (type a, b)	2.60	2.62
Dense (type c,d)	2.32	2.34
P	.032	.022

Table 2. Diagnostic Efficiency of Diffusion MRI According to BI-RADS Scoring in Different Breast Densities BI-RADS Score

	R1			R2		
	Sensitivity	Specificity	AUC	Sensitivity	Specificity	AUC
Non-dense	86%	45%	0.820	94%	56%	0.827
Dense	93%	54%	0.893	92%	65%	0.901
P	.395	.590	.184	.886	.575	.167

Table 3. Diagnostic Efficiency of Diffusion MRI Calculated from ADC Value at Different Breast Densities ADC

	R1			R2		
	Sensitivity	Specificity	AUC	Sensitivity	Specificity	AUC
Non-dense	79%	65%	0.704	88%	59%	0.782
Dense	89%	72%	0.805	97%	70%	0.835
P	.228	.645	.154	.135	.420	.401

specimens, while 27 cases were diagnosed based on stable lesion characteristics observed for over 2 years.

Lesions characterized as focus and non-mass enhancement, cysts, and patients who had undergone neoadjuvant chemotherapy were excluded from the study.

Magnetic Resonance Imaging Protocol

Imaging was performed on 1.5T MRI systems (Siemens Magnetom Symphony and Aera; Siemens Healthcare, Erlangen, Germany) using dedicated phased-array breast coils.

The imaging protocol included T2-weighted (TR/TE, 4000/70 ms; FOV read 350; 3 mm thickness; number of slices 20), dynamic contrast-enhanced T1-weighted (TR/TE, 700/12 ms; FOV read 350; thickness 2 mm; number of slices 30), and diffusion-weighted sequences (DWI technical parameters; 4-channel coil, axial plan, Diffusion MRI sequence—2B SE-EPI; TR/TE 5400/94; Slice thickness 3 mm; In-plane resolution (mm); 1.7×1.7 ; Matrix 192×192 ; Fat Suppression; Bandwidth (BW) 1370; b value 50, 400, 1000; Acquisition time (min) 2.38).

For dynamic contrast enhancement, 0.1 mmol/kg body weight of gadolinium-based contrast agent was administered intravenously at a rate of 2 mL/s, followed by a 20-mL saline flush. Diffusion-weighted imaging was acquired prior to dynamic contrast-enhanced imaging. Apparent diffusion coefficient maps were automatically generated.

Qualitative Analysis of Magnetic Resonance Imaging

Image interpretation was performed independently by 2 experienced radiologists (Radiologist H.A.A.K. with 20 years and Radiologist S.K. with 25 years of breast MRI experience) on a Leonardo workstation (Siemens Healthcare).

MAIN POINTS

- This study reveals diffusion-weighted magnetic resonance imaging (DWI-MRI) demonstrates high diagnostic efficacy in both dense and non-dense breasts, offering a promising tool for breast cancer detection.
- Despite higher tumor visibility in non-dense breasts, the diagnostic accuracy was not significantly affected by breast density.
- The DWI-MRI can be a valuable adjunct to mammography, especially in challenging cases such as dense breasts.

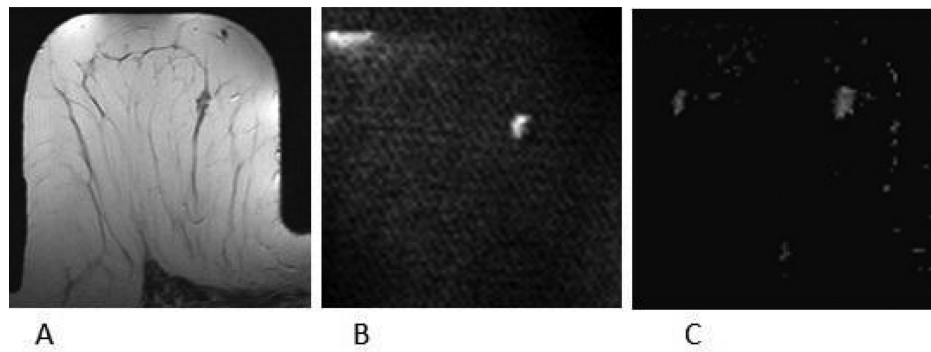


Figure 1. Invasive ductal carcinoma of 11 mm. An irregularly shaped mass is visible on the T2-weighted image (A). The mass is highly visible and has high DWI signal as seen on the high b value image. Malignancy score was 5-6 on qualitative assessment (B). The ADC value of the mass was measured as $0.95\text{--}1.02 \times 10^{-3} \text{ mm}^2/\text{s}$ on ADC map (C).

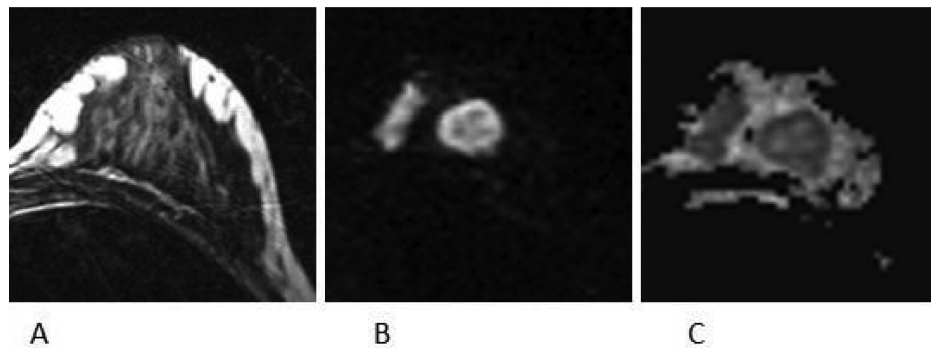


Figure 2. Invasive ductal carcinoma of 21 mm. Due to dense breast pattern tumor is not visible on the T2-weighted image (A). The mass is highly visible and has high DWI signal on the high b value image. Malignancy score was 7 (B). The ADC value was $0.56\text{--}0.72 \times 10^{-3} \text{ mm}^2/\text{s}$, measured on the ADC map (C).

Evaluations for DWI were conducted in separate sessions separated by a 3-week interval. Throughout the interpretation process, the radiologists remained blinded to clinical information and final diagnostic outcomes.

Evaluation parameters included tumor visibility (scored on a 4-point scale: 0 = not seen, 1 = poor, 2 = moderate, 3 = high), Breast Imaging Reporting and Data System (BI-RADS) score, and tumor ADC value. Each case was evaluated based on a single, index lesion that was considered to be the most suspicious.

The BI-RADS score (7-point scale) (citation BI-RADS 2013) was determined considering the morphological features of the tumor on diffusion-weighted images and the signal intensity on the ADC map. Tumor ADC values were measured from the ADC maps. The effectiveness of tumor visibility and characterization in different breast densities (a, b = non-dense; c, d = dense) was compared using Student's *t*-test, chi-square test, and receiver operating characteristic (ROC) analysis.

Quantitative Analysis of Magnetic Resonance Imaging

Tumor size and ADC values were assessed by a single radiologist (X) following the completion of morphologic evaluations. This assessment constituted the final stage of the independent reading sessions conducted by this radiologist. Tumor size was determined on the axial slice demonstrating the largest tumor dimension.

The ADC values were measured on ADC maps utilizing circular regions of interest encompassing at least 3 pixels. Measurements were acquired from the region within the tumor exhibiting the most pronounced diffusion restriction. A minimum of 3 measurements were performed, and the lowest value was utilized for subsequent analysis.

Statistical Analysis

Statistical analyses were conducted using SPSS Statistics version 23.0 (IBM SPSS Corp.; Armonk, NY, USA).

Inter-method and inter-reader agreement was assessed using Cohen's kappa statistics. Kappa values were calculated 0.597, $P < .001$. The discriminative ability of DWI parameters was evaluated using ROC curve analysis. Sensitivity, specificity, and area under the curve (AUC) values were calculated for each MRI system to assess the diagnostic performance.

Statistical significance was defined as a *P*-value less than .05.

RESULTS

A total of 86 benign and 130 malignant cases were included in the study. One hundred and sixteen cases had dense breast parenchyma, while 100 had non-dense parenchyma. The mean tumor visibility score on DWI-MRI was significantly higher in non-dense breasts compared to dense breasts ($P < .03$) (Table 1). The diagnostic performance of DWI for

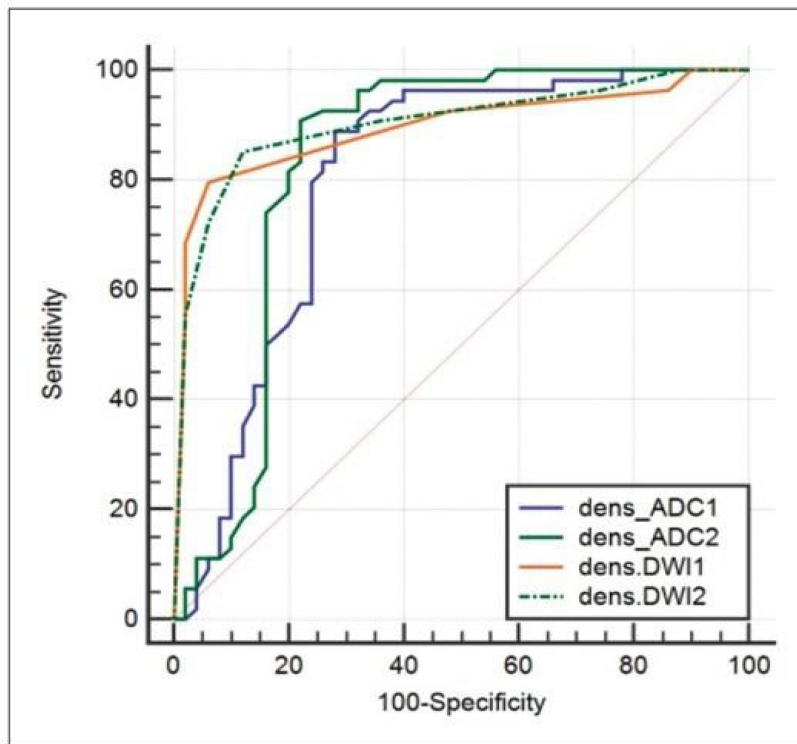


Figure 3. Sensitivity, specificity, and diagnostic accuracies (AUC value) were calculated from the BI-RADS score and ADC value of dense breast densities. No difference was found in the sensitivity, specificity, and AUC value calculated from the BI-RADS score and ADC value in different breast densities ($P > .05$).

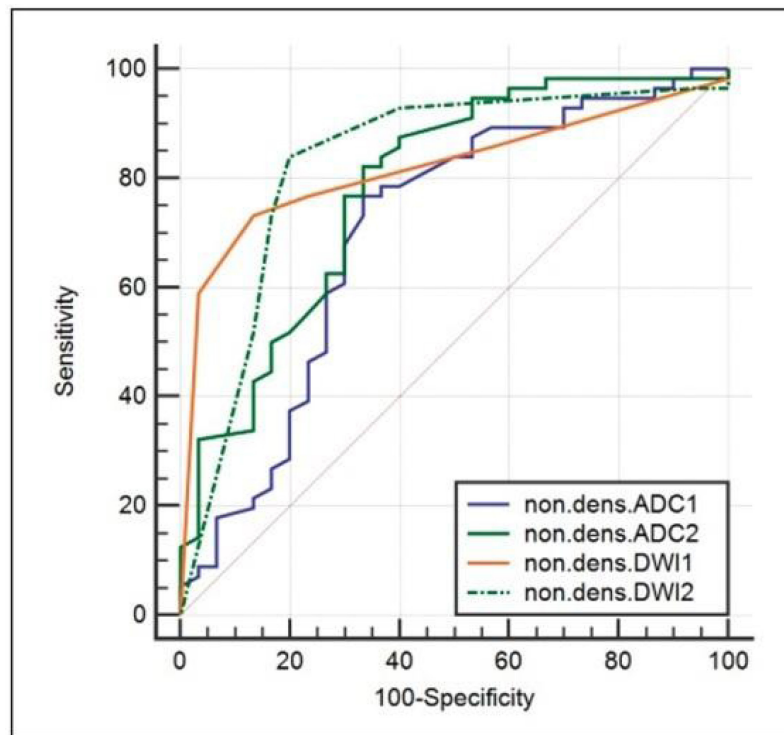


Figure 4. Sensitivity, specificity, and AUC value calculated from the BI-RADS score and ADC value of non-dense breast densities. No difference was found in the sensitivity, specificity, and AUC value calculated from the BI-RADS score and ADC value in different breast densities ($P > .05$).

cancer detection was calculated 89%-97% in dense breasts and 79%-94% in non-dense breasts (Figures 1 and 2). However, there were no significant differences in sensitivity, specificity, and diagnostic accuracy (AUC value) based on BI-RADS score (Table 2) and ADC value (Table 3) across different breast densities ($P > .05$) (Figures 3 and 4).

The mean ADC value was significantly lower in malignant tumors compared to benign tumors ($P < .001$).

There was a moderate level of inter-observer agreement in BI-RADS assessment ($\kappa=0.597$, $P < .001$).

DISCUSSION

The results indicate that DWI-MRI can effectively visualize and characterize breast lesions without being influenced by breast fibroglandular tissue density. This conclusion is supported by the observation of significantly lower mean ADC values in malignant lesions compared to benign lesions.

These findings corroborate the observations of previous research which demonstrated diminished ADC values in malignant breast neoplasms.¹ This reduction is attributed to the increased cellular density and restricted water movement within these tumors.

The DWI-MRI is an advanced radiological imaging technique with high efficacy in characterizing breast tumors even in dense breasts. By evaluating the ADC value and tumor morphological features, benign and malignant tumors can be differentiated with 80%-90% accuracy. However, the diagnostic accuracy of DWI-MRI is influenced by various technical and patient-related factors.

Breast fibroglandular tissue density, a significant patient-related variable, is a major determinant of diagnostic efficacy in mammography. Effective fat suppression in DWI-MRI is indispensable for enhancing tumor visibility and reducing artifacts. While it might be expected that DWI-MRI would have reduced diagnostic efficacy in breasts with excessive fatty tissue due to suppression issues and artifacts, this study demonstrated that the diagnostic efficacy of DWI-MRI is not affected by breast density and tumor visibility is higher in fatty breasts.

In a retrospective study performed by Wielema et al⁹ in 400 consecutive patients with no history of breast surgery or breast implants, dense breasts were found to have excellent fat suppression and significantly higher DWI image quality than non-dense breasts. The findings provide further evidence in support of the conclusions drawn in this study with quantitative ADC calculations.

According to this study results, DWI-MRI demonstrates a high sensitivity for the detection of malignant breast tumors, independent of breast fibroglandular tissue density.

Tumor visibility and the diagnostic accuracy of DWI are not influenced by fibroglandular tissue density.

This retrospective study has several limitations. The distribution of benign and malignant tumors may not be representative of the general population, and histopathological correlation was lacking in 27 cases.

Additionally, the study's focus was limited to index tumors. Larger-scale studies are required to fully document the efficacy of DWI in all its applications.

Diffusion-weighted MRI can serve as a valuable adjunct to conventional mammography in improving the detection of breast cancer, particularly in women with dense breasts.

The diagnostic efficacy of DWI-MRI is unaffected by breast fibroglandular tissue density. Diffusion-weighted imaging demonstrates a high detection rate of cancer in dense breasts, making it a potential alternative to mammography in clinical settings where mammography is less effective.

Data Availability Statement: The data that support the findings of this study are available on request from the corresponding author.

Ethics Committee Approval: This study was approved by the ethics committee of Karadeniz Technical University (Approval No: 2025/16 Date: 25.03.2025).

Informed Consent: Written informed consent was obtained from the patients who agreed to take part in the study.

Peer-review: Externally peer-reviewed.

Author Contributions: Concept – S.K.; Design – H.A.A.K., S.K.; Supervision – S.K., H.A.A.K.; Resources – H.A.A.K.; Materials – S.K., H.A.A.K.; Data Collection and/or Processing – S.K., H.A.A.K.; Analysis and/or Interpretation – S.K., H.A.A.K.; Literature Search – H.A.A.K.; Writing Manuscript – H.A.A.K.; Critical Review – S.K., H.A.A.K.

Declaration of Interests: The authors have no conflict of interest to declare.

Funding: The authors declared that this study has received no financial support.

REFERENCES

1. Şenbil DC, Bilici E, Kösetürk T, Çetin T. Breast imaging with diffusion-weighted magnetic resonance imaging: evaluating apparent diffusion coefficient values and biomarker expression in benign and malignant lesions. *Curr Res MRI*. 2023;2(3):50-54.
2. Duijm LEM. Dense breasts at breast cancer screening: can DWI-based breast MRI without contrast help us in the pursuit of personalized screening? *Eur Radiol*. 2024;34(7):4727-4729. [\[CrossRef\]](#)
3. Baltzer PAT, et al. Breast cancer screening in women with extremely dense breasts — recommendations of the European Society of Breast Imaging (EUSOBI). *Eur Rad*. 2022;32(9):6039-6048.
4. Rahmat K, Mumin NA, Hamid MTR, Hamid SA, Ng WL. MRI breast: current imaging trends, clinical applications, and future research directions. *Curr Med Imaging*. 2022;18(13):1347-1361. [\[CrossRef\]](#)
5. McCormack VA, dos Santos Silva I. Breast density and parenchymal patterns as markers of breast cancer risk: a meta-analysis. *Cancer Epidemiol Biomarkers Prev*. 2006;15(6):1159-1169. [\[CrossRef\]](#)
6. Partridge SC, DeMartini WB, Kurland BF, Eby PR, White SW, Lehman CD. Quantitative diffusion-weighted imaging as an adjunct to conventional breast MRI for improved positive predictive value. *AJR Am J Roentgenol*. 2009;193(6):1716-1722. [\[CrossRef\]](#)
7. Kul S, Cansu A, Alhan E, Dinc H, Gunes G, Reis A. Contribution of diffusion-weighted imaging to dynamic contrast-enhanced MRI in the characterization of breast tumors. *AJR Am J Roentgenol*. 2011;196(1):210-217. [\[CrossRef\]](#)
8. Kul S, Metin Y, Kul M, Metin N, Eyuboglu I, Ozdemir O. Assessment of breast mass morphology with diffusion-weighted MRI: beyond apparent diffusion coefficient. *J Magn Reson Imaging*. 2018;48(6):1668-1677. [\[CrossRef\]](#)
9. Wielema M, Sijens PE, Pijnappel RM, et al. Image quality of DWI at breast MRI depends on the amount of fibroglandular tissue: implications for unenhanced screening. *Eur Radiol*. 2024;34(7):4730-4737. [\[CrossRef\]](#)